

HfO₂, Al₂O₃, and ZnO Based Metal-Insulator-Metal Photovoltaic Structures for Solar Cell Applications

by
EMRE CAN DURMAZ

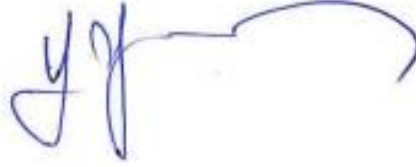
Submitted to the Graduate School of Engineering and Natural Sciences
in partial fulfillment of
the requirements for the degree of
Master of Science

Sabanci University,
Summer, 2018

HfO₂, Al₂O₃ and ZnO Based Metal-Insulator-Metal Photovoltaic Structures for Solar Cell Applications

APPROVED BY:

Prof. Dr. Yaşar GÜRBÜZ
(Thesis Supervisor)



Assist. Prof. Murat Kaya YAPICI



Assoc. Prof. Serkan TOPALOĞLU



DATE OF APPROVAL: 31/07/2018

© Emre Can Durmaz 2018

All Rights Reserved

Acknowledgments

First and foremost, I would like to thank my advisor Prof. Yasar Gurbuz for his encouragement and constant support during my undergraduate and master's studies at Sabanci University. It is my privilege to be part of his team and be able to finish my master's studies under his supervision.

I would like to thank the members of my thesis committee, Assist. Prof. Murat Kaya Yapici, and Assoc. Prof. Serkan Topaloglu for their helpful comments and for their time.

I would like to thank my friend and colleague, Elif Gul Arsoy, Hamza Kandis, Esref Turkmen, Dr. Melik Yazici, Dr. Omer Ceylan and Ali Kasal for their support and contribution to this work.

I also would like to express my special thanks to my friends Abdurrahman Burak, Alper Guner, Atia Shafique, Can Caliskan, Cerin Ninan Kunnatharayil, Ilker Kalyoncu, Shahbaz Abbasi, Tahsin Alper Ozkan for creating such a friendly and enjoyable working environment.

I thank my friends Deniz, Onur, Cagri, Basak, Oytun, Furkan, Omer, Harun, Canberk for their friendship. They made my life easy and full of fun.

Most of all, I am grateful to my family, my sister Esra, and my parents Suleyman and Serife, and my brother Kaan for their unconditional love, endless support and for always believing me. I would not come that far without the sacrifices they made.

HfO₂, Al₂O₃, and ZnO Based Metal-Insulator-Metal Photovoltaic Structures for Solar Cell Applications

Emre Can Durmaz

EE, Master's Thesis, 2018

Thesis Supervisor: Prof. Dr. Yasar Gurbuz

Keywords: MIM diode, hot electrons, photovoltaic effect, quantum tunneling, solar cell.

Abstract

Currently, the solar cell market is dominated by silicon-based solar cell since the bandgap of the silicon is an appropriate match to solar spectrum and silicon is most abundant material on the earth. However, the efficiency of the silicon-based solar cells is limited hence the research and development are concentrated on alternative methods.

The Metal-Insulator-Metal(MIM) diode consists of an insulator layer sandwiched between two metals. The current generation mechanism is based on the photovoltaic effect that enables to form Metal-Insulator-Metal solar cells. The technological development allows leading investigations about developing highly efficient MIM diode promising broad applications.

MIM diodes have several advantages such as low cost, potentially having high conversion efficiency, integrated circuit (IC) compatibility. Therefore, the feasibility of MIM diodes for solar cell application is explored. In the MIM diode, insulator layers are an integral part of the devices, preponderantly determining the performance parameters. MIM diodes with different material selections based on three insulators (HfO₂, Al₂O₃, and ZnO) and three metals (Au, Cr, and Ni) are evaluated to compare performance parameters, with conversion efficiency being prioritized. Based on the responsivities of the devices, the HfO₂-based MIM diode gives the highest efficiency under visible light due to the fact that hot electron and leading electrons tunnel through thin energy barrier more asymmetric than the other MIM diodes enabling more number of hot electrons tunneling through. Hence insulating layer is a critical parameter in terms of tunneling probability of hot electrons and optimizing conversion efficiency. At the end of this study, Metal Insulator Metal structure is combined with a converter module that charges a battery that demonstrates the feasibility of MIM solar cell.

Güneş Hücresi Uygulamaları için HfO₂, Al₂O₃ ve ZnO Bazlı Fotovoltaik Metal-Yalıtkan-Metal Yapıları

Emre Can Durmaz

EE, Yüksek Lisans Tezi, 2018

Tez Danışmanı: Prof. Dr. Yaşar Gürbüz

Anahtar Kelimeler: Metal Yalıtkan Metal yapıları, sıcak elektronlar, fotovoltaik etki, quantum tünellemesi, güneş hücresi

Özet

Silikon bant aralığının güneş spektrumuna tam olarak uygun düşmesi ve silikonun dünya üzerinde en çok bulunan elementlerden biri olması sebebi ile günümüz güneş hücreleri marketine silikon bazlı güneş hücreleri hakimdir. Ancak silikon güneş hücrelerinin verimliliği sınırlıdır. Bu yüzden araştırma ve geliştirme alternatif metotlara yoğunlaşmıştır.

Metal Yalıtkan Metal diyotlar, iki metal arasında bulunan ince yalıtkan katmandan oluşur. Metal Yalıtkan Metal diyotun fotovoltaik etki ve kuantum tünellemesi üzerine kurulu akım üretim mekanizması, bu diyotlar ile güneş hücresi oluşturmaya olanak sağlar. Teknolojik gelişmeler, yüksek verimli Metal Yalıtkan Metal diyotlarının üretimini ve geniş kullanım alanları için araştırılmasını mümkün kılmaktadır.

Metal Yalıtkan Metal diyotları; düşük maliyet, yüksek çevirme verimine sahip olma potansiyeli ve entegre devreler ile uyumluluk gibi avantajlara sahiptir. Bu yüzden, tez çalışması kapsamında Metal Yalıtkan Metal diyotlarının güneş hücreleri için uygunluğu incelenmiştir. Metal Yalıtkan Metal yapısındaki yalıtkan tabaka performans parametrelerini baskın bir şekilde belirleyen ayrılmaz bir parçadır. Çalışma kapsamında, 3 farklı yalıtkan (HfO₂, Al₂O₃, ve ZnO) ve 3 farklı metalden (Au, Cr, ve Ni) oluşan farklı materyal seçimli Metal Yalıtkan Metal yapılarının performansları, verimlilik öncelikli olacak şekilde, karşılaştırılarak değerlendirilmiştir. Cihazların duyarlılıklarının baz alındığı durumda HfO₂ bazlı Metal Yalıtkan Metal yapısının, görünür ışık altında en fazla verimliliğe sahip olduğu görülmüştür. Bunun sebebi asimetrik bariyer formasyonunun diğer yapılara oranla, ince enerji bariyerinden daha fazla sıcak elektronun tünelleme yapmasına olanak sağlamasıdır. Dolayısıyla yalıtkan tabaka, verimliliği optimize etmek ve sıcak elektronların tünellemesi için kritik parametredir. Bu çalışmanın sonunda Metal Yalıtkan Metal yapısının, bir pil doldurmaya yarayan çevirici module bağlanarak, güneş hücresi yapımına uygun olduğu gösterilmiştir.

Contents

Acknowledgments	iv
Abstract.....	v
Özet.....	vi
Contents	vii
List of Figures.....	ix
List of Tables	xi
List of Abbreviations	xii
1. Introduction	1
1.1. Solar Cell.....	1
1.2. Introduction to Metal Insulator Metal Diode	3
1.3. Motivation	4
1.4. Organization.....	5
2. Fundamentals of MIM diode	7
2.1. MIM diode Operation	7
2.2. Quantum Tunneling and Energy Band Diagram.....	8
2.3. Photovoltaic Effect in MIM – Hot Electron.....	11
3. Experimental MIM diode	13
3.1. Design of the MIM diode	13
3.1.1 Single MIM diode.....	13
3.1.2 Array Format of MIM diode.....	16
3.1.3 Verification MIM diodes Optical Response.....	16
3.2. Fabrication.....	18
3.2.1 Electron Beam Lithography	19
3.2.2 Deposition of the Materials	20
3.2.3 Atomic Layer Deposition (ALD)	21
3.2.4 Mask Layouts	22
3.3. Characterization	25
3.3.1 Physical Characterization	25
3.3.2 Electrical Characterization	27
3.3.2.1 Measurement Results of Single MIM diodes	28
3.3.2.2 Measurement Results of 10x10 Array MIM diodes	32
3.3.2.3 Measurement Results of Verification MIM diodes Optical Response ...	34
3.4. Efficiency Calculation.....	36
4. Stand Alone Converter Evaluation Module Design	43

4.1.	Operation of Ultra Low power Step up Converter.....	43
4.2.	Design	45
4.3.	Measurement Results	48
5.	Conclusion & Future Work	50
5.1.	Summary of Work.....	50
5.2.	Future Work	51
	REFERENCES	53

List of Figures

Figure 1	Energy Band Diagram of Metal-Insulator-Metal Diode with an applied bias voltage.....	8
Figure 2	Design of a single MIM diode	14
Figure 3	Conduction band diagram of an asymmetric barrier tunnel barrier with a barrier height of the MIM diodes.....	15
Figure 4	The layout and schematic of the 10x10 array.....	17
Figure 5	The design of the without MIM diode.....	17
Figure 6	The representation of the fabrication steps in terms of material deposition.....	18
Figure 7	The optical microscope image of the structures after the first step of EBL and development.	20
Figure 8	SEM image of the MIM diode.....	22
Figure 9	The mask for Cr/HfO ₂ /Ni samples	23
Figure 10	The mask for Au/Al ₂ O ₃ /Ni and Au/ZnO/Ni samples	24
Figure 11	The mask for without MIM diode.....	24
Figure 12	EDX Spectroscopy results of the Cr/HfO ₂ /Ni structure	25
Figure 13	The ellipsometry results of the MIM diodes and bare GaAs substrate.....	26
Figure 14	DC characterization setup.....	27
Figure 15	The spectrum of the halogen lamp.....	28
Figure 16	I-V characteristic of Au/Al ₂ O ₃ /Ni with respect to the illumination.....	30
Figure 17	I-V characteristic of Au/ZnO/Ni with respect to the illumination.....	30
Figure 18	I-V characteristic of Cr/HfO ₂ /Ni with respect to the illumination.....	31
Figure 19	The responsivity of the structures with respect to the insulator layer	31
Figure 20	I-V characteristic of 10x10 array with respect to optical intensity.....	33
Figure 21	Current change vs. Optical intensity with respect to different bias voltages.....	33
Figure 22	I-t sampling at constant 1V in order to show repeatability.....	34
Figure 23	I-V characteristics of without insulator layer with respect to optical radiation.....	35
Figure 24	The comparison of the without MIM diode and MIM diode.....	35
Figure 25	Circuit diagram of the measurement setup	37
Figure 26	Isolated load box in order to obtain output power from MIM diode.....	37

Figure 27	Efficiency measurement setup with the illumination of 625 nm LED	39
Figure 28	Variable R_{load} test to find maximum power transfer	40
Figure 29	The circuit diagram of the low noise instrumentation amplifier design for efficiency calculation	41
Figure 30	Efficiency measurement with advanced setup for Halogen Lamp	42
Figure 31	Efficiency measurement with advanced setup for 625 nm LED	42
Figure 32	Working chain of the converter module	43
Figure 33	Block diagram of the LTC 3108 [58]	44
Figure 34	Schematic of the converter module design	46
Figure 35	The layout of the converter module design	46
Figure 36	Frontside of the 3 D model of the design.....	47
Figure 37	The backside of the 3 D model of the design	47
Figure 38	The diagram of the matching circuit.....	48
Figure 39	The measurement result of the converter module that multimeter show 5V.....	49

List of Tables

Table 1	Metal Deposition Parameters	21
Table 2	Efficiency Measurement Results for Single MIM diode.....	38
Table 3	Efficiency Measurement Results for 10x10 MIM diode.....	39

List of Abbreviations

AC	Alternative Current
ACE	Acetone
ALD	Atomic layer deposition
DC	Direct Current
DEZ	Diethylzinc
EBL	Electron beam lithography
EDX	Energy Dispersive X-ray Spectroscopy
IC	Integrated circuit
IPA	Isopropanol
IR	Infra-Red
MIBK	Methyl-isobutyl-ketone
MIM	Metal-insulator-metal
MOM	Metal-Oxide-Metal
PMMA	Electron resist polymethyl methacrylate
PVD	Physical Vapor deposition
SEM	Scanning Electron Microscope
SMU	Source/Measure Units
TMA	Trimethylaluminum
TMM	Transfer Matrix Method
WKB	Wentzel-Kramers-Brillouin

1. Introduction

1.1. Solar Cell

Increasing demand for energy has led scientists to conduct intense and continuous research about renewable and environmentally clean energy sources such as solar, wind, hydro, thermal and biomass. Solar cells, firstly invented by Edmon Becquerel in 1839, are one of the primary renewable energy sources being focused for investigation because of several factors such as the limitless source of the sun, potential improvements on fabrication cost and efficiency. In other words, collecting solar energy and generating electricity from solar energy have broad applications and attracts the attention of the researchers.

The first advantage of the solar cell is the limitless source of the sun [1]. Solar energy reaches the surface of the earth in the form of heat and radiations at a rate of 120 petaWatt (10^{15} Watt), which corresponds energy demand of the World for 20 years [2].

The most popular material for solar cells is silicon since the bandgap is an appropriate match to solar spectrum [3]. Silicon is one of the most abundant elements on the earth therefore in terms of cost; solar cells have a significant advantage. Moreover, solar energy is clean and renewable. It does not emit carbon dioxide during operation that is why solar cells do not threaten the environment.

The efficiency of the solar cells is the main topic of the researches for decades. Single crystalline silicon-based photovoltaic cells are the most conventional solar cells because of the relation between bandgap and the solar spectrum. However, the limitations of single crystalline solar cells were investigated and reported [3]-[5]. The fundamental limit of these solar cells is originated from the current generation mechanism that depends on electron excitation by the incident photons whose energy is greater than the bandgap of the material. Electrons on the valence band state move across conduction band state by creating a hole on the valence band through the energy of the incident photon. However, some excited electrons can lose power thermally before the conduction band edge or recombination process occurs. As a result, incident photon energy dissipates without

generating electron-hole pair and the efficiency decreases [7]. Although 90% of the solar cell market is based on silicon, different materials and techniques are investigated for more efficient and lower cost technology [8].

The state of the art single junction crystalline silicon cell has the 27.2% maximum efficiency value [9], as the multi-crystalline silicon cells reported a 22.3% efficiency value [10]. Although the multi-crystalline silicon cells lead the decrease in efficiency because of having disorder atomic structure, they have an advantageous characteristic such as low cost and durability to degeneration because of the radiation promising long lifetime.

Another low-cost technology for solar cells is thin films that depend on the deposition of photosensitive materials such as a-Si, Cadmium Telluride (CdTe), Copper Indium-Gallium-Arsenide (CIGS) [11]. The advantage of these solar cells is expending low raw materials during fabrication because of the thickness of the films is in the micrometer range. The efficiency of II-VI semiconductor thin film is maximum 23% [12], as III-V semiconductor thin film cells such as GaAs, InP has 25.1 % [13] and 24.2% efficiency [14]. On the other hand, a-Si cells have only 10.2% efficiency [15]. The disadvantages of thin film solar cells are occupying the vast land, short lifetime [2].

The multi-junction solar cell is one of most popular technique to develop efficient solar cells. The multi-junction solar cells are based on the formation of multiple p-n junctions between different semiconductor materials. Each junction in the solar cell structure corresponds to the different wavelength that provides broadband spectrum response. The absorption of different wavelength radiation enhances the efficiency of the solar cell. Most popular material selection for the multijunction is III-V semiconductors. The maximum efficiency values are 46% with GaInP/GaAs; GaInAsP/GaInAs structures [16] and 45.7% with GaInP/GaAs/GaInAs/GaInAs structures [17]. The drawback of this type of structure is mainly fabrication costs. Therefore the applications are limited. Moreover, the structures usually contain poisonous materials such as GaAs, CdTe; and the environment can be harmed if these materials are leaked [2].

There are also dye-sensitized, organic photovoltaic, perovskite, quantum dot photovoltaic, chalcogenide solar cells under research and development [18], [19] other than the mentioned technologies and any of which does not exceed the efficiency of silicon-based solar cells. Only perovskite solar cell efficiency is close to silicon-based

solar cells with 22.7% [20]. However, drawbacks of the solar cells at present induces to research alternative methods.

1.2. Introduction to Metal Insulator Metal Diode

Metal-Insulator-Metal(MIM) is a structure formed by nano-scale insulator layer sandwiched between two metal layers. The first attention for investigation of MIM diodes started in 60's [21]-[23]. However, improvements in fabrication and nanotechnology capabilities have led these devices to be suitable for different applications, in recent decades. Through the insulator layer between metals that enables thin energy barrier, electron tunneling mechanism in the nano-scaled MIM diodes provides advantages for specified applications.

Infrared Detection is one of the prevalent applications of MIM diodes. Reported research shows that thin film MIM diodes can be utilized for IR detection. Wiesendanger (1977), stated that thin film metal-oxide-metal tunnel junctions formed by different metals and their native oxides generate conventional point contact diodes that act as infrared detectors with non-linear response [24]. Heiblum (1978) presented that metal oxide metal structure formed by Ni/NiO/Ni exhibits detection performance for Near IR range, and the structures were stable and successfully fabricated reproducibly unlike the point contact diodes [25]. Similarly, Wilke (1994) reported the design and the performance of the antenna coupled Ni/NiO/Ni structure for Long Wave IR (LWIR) detection [26]. Fumeaux (1998), then, enhanced the performance of the structure, [27]. On the other hand, it is seen that the investigation of metal insulator metal infrared detectors intensified due to the improvement in fabrication ability. For instance, Pashang Esfandari (2005) proposed that Metal Oxide Metal structure coupled with a tunable antenna can be utilized as uncooled IR detector for military applications since it offers multispectral sensing without the need of cryocooling system that decreases the overall cost of the system [28]. Highly sensitive thin film Ni/NiO/Cr structure that was proposed for Far IR detection by Krishnan (2008) [29]. Gadalla (2014) showed that by using state of the art fabrication techniques, nano-scaled device structures and even less than 1 nm insulator thickness could be obtained in a MIM rectifier that has high responsivity and low zero bias resistance [30]. According to those researches, it can be concluded that MIM diodes are preferable in terms of ultra-fast response time thanks to quantum tunneling, although the MIM IR detection has low responsivity and detectivity in comparison to other IR detectors.

Energy harvesting is another major application of MIM diodes. MIM diodes are mostly utilized as rectifier part of the optical rectennas. Rectennas were firstly proposed for microwave power transmission or wireless power transmission systems [21]. In rectennas, antenna part absorbs incoming RF energy and rectifier part converts it to usable DC power. The idea of using rectennas for solar energy conversion was invented by Bailey [31]. However, the improvement in fabrication ability has been suitable MIM diodes for solar cell rectenna. There are many studies of rectenna for energy harvesting and solar cell applications [32-36]. However, rectenna is not the only way for solar energy conversion with MIM diodes. Hot electron based MIM diodes are analyzed for solar cell applications.

There are many studies about hot electrons and the current mechanism of the devices for planar MIM diodes in terms of the energy barrier [37-42]. In 1975, Burshtein defined that Al-Al₂O₃-Au based MIM diodes had a Photo-Induced Tunnel Current and stated hot electron theory in these devices [37]. Then Marshalek analyzed the theory experimentally and also presented the energy loss of electrons due to inelastic collisions [38]. Furthermore, hot electron generation by exciting the surface plasmons under infrared light has been demonstrated in metal-semiconductor based Schottky barrier [39]. Also, the hot electron current generation mechanism has been shown by keeping the top and bottom metals same and reshaping one of the top metal layers with plasmonic stripe antenna. It shows that excited surface plasmons can be manipulated to enhance the photocurrent [40]. Moreover, the conversion efficiency of the MIM hot electron based surface plasmons (SPs) is calculated theoretically and demonstrated experimentally under different wavelength illumination by using a prism [41]. Brongersma et al. have emphasized the advantages of the plasmon-induced hot carriers in terms of increasing light absorption and conversion into the current [42].

1.3. Motivation

MIM diodes have current generation mechanism that can be evaluated as the photovoltaic effect. The structures are suitable to fabricate conveniently due to the technological developments and cost of the materials are considerably low since the fabricated structures are nano-scaled. Besides, the process is compatible with integrated circuits. All these advantages enable to form MIM diode based photovoltaic solar cells. Although MIM diode based photovoltaic cell can barely compete with silicon solar cell in terms of cost, because of the efficiency limitations of the silicon solar cell, MIM diode based

photovoltaic cell is one of a decent potential candidate for an alternative solar cell that may be able to substitute silicon solar cells by promising improvements on conversion efficiency.

The primary objective of the thesis is to investigate the feasibility of the MIM diodes for solar cell applications. In order to fulfill this objective, the design, fabrication, and characterization of different MIM diodes are aimed. Firstly, the design of the single MIM diode is conducted to decide suitable material selection. After the fabrication of these designed MIM diodes, the characterization of these devices is evaluated regarding the optical response.

The target is to develop highly efficient MIM diode to convert optical radiation to DC energy. The investigation is focused on, firstly material selection specifically insulator layer. Secondly, the factors that possibly improve the performance of the devices are aimed to analyze such as array formation and fabrication abilities. The evaluation of the results is another significant milestone of this research. That is why a custom design measurement setup is constructed by considering external electrical power transfer. Finally, an energy harvester demonstration is planned to perform with an evaluation module design.

1.4. Organization

The thesis is organized as follows. Chapter 2 introduces the fundamentals of the operation of MIM diodes. Current generation mechanism is analyzed during this chapter. A comprehensive literature review about working principle and the concept of hot electron based MIM diodes are presented. Conducted researches about hot electron based MIM diodes are examined by focusing on the suitability for solar cell applications.

In Chapter 3, the design of different MIM diodes is shown by explaining the consideration during the structural design process. Material selection and the band diagram are analyzed. After that, fabrication methods and steps of MIM diodes are presented, and the fabrication process is detailed. Physical and electrical characterization of the devices is reported in this chapter. Optical response of the illuminated MIM diodes and the I-V characteristics are investigated. Finally, to evaluate the efficiency of the devices, designed the measurement setup and the efficiency calculation are explained.

In Chapter 4, the design of a converter module is presented. The module is a demonstration of the ability of MIM diode based solar energy harvester. For this purpose, LTC 3108, a low power step-up DC to DC converter integrated circuit, a product of Analog Devices is used. The operation of the integrated circuit is explained in detail in this chapter. The design of the module is performed with KiCAD program. The measurement result is also reported in this chapter. With this module, photon generated current of the MIM diodes is converted to an output that is suitable to charge a battery.

2. Fundamentals of MIM diode

In this chapter, firstly MIM diode operation is defined. The working principle and the current generation mechanism for unilluminated MIM diodes are expressed with equations. Then, quantum tunneling phenomena for this type of structure is theoretically conceptualized with energy band diagram. The derivation of quantum tunneling current and the approximation methods are presented. In addition, the illumination effect on the quantum tunneling is analyzed. Finally, hot electron carriers in MIM diodes and the photovoltaic effect due to the hot electrons is investigated.

2.1. MIM diode Operation

Metal Insulator Metal (MIM) structure consists of two metal layers and a thin insulator layer between the metals. The metals could be either same, for symmetric MIM or different for asymmetric MIM. The dominant carrier transport mechanism is quantum tunneling for thin insulator layer. Although growing native oxide on top of the bottom metal was preferable for conventional MIM diode because of relatively easy fabrication techniques for oxidation process, with the development of fabrication technology, various thin insulator layer deposition for MIM diodes has become prevalent.

Three different factors describe the energy band diagram of the MIM diode. Those are the first metal's work function (ψ_{M1}), which is the potential difference between vacuum level and Fermi level (E_f) of the metal, insulator layer's electron affinity, which is the potential difference between vacuum level and conduction band of the insulator layer and the second metal's work function (ψ_{M2}). For the equilibrium condition, the band diagram is shown in Figure 1.

The quantum tunneling occurs when the electron passes through insulator layer from one metal to the other metal. In equilibrium condition, there is quantum tunneling with low probability. However, when the bias applied the Fermi level of the metal is modulated as shown in Figure 1. The transmission distance that the electron tunnels decreases. The shape of the diagram becomes more asymmetric than previous. The tunneling probability increases hence the tunneling current increases.

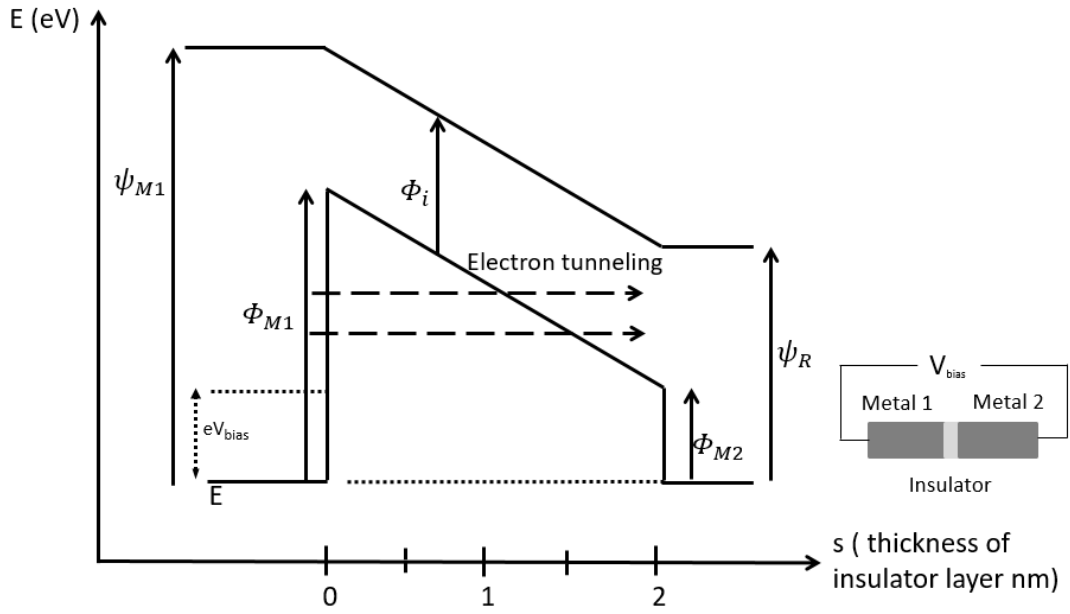


Figure 1 Energy Band Diagram of Metal-Insulator-Metal Diode with an applied bias voltage

2.2. Quantum Tunneling and Energy Band Diagram

The tunneling current is calculated by the amount of the electron that tunnels through insulator layer in a second. Hence, the current density(J) is proportional to charge velocity (v) and the carrier concentration(n) at the electron energy E . The current density is expressed as [43];

$$J = -qnv = -qn(E)v(E)T(E) \quad (1)$$

where the q is charge and $T(E)$ is the tunneling probability. The carrier concentration equals to multiplying of the density of the states $g(E)$ and the Fermi distribution function $f(E)$ [44].

$$n(E) = g(E)f(E) \quad (2)$$

The density of the state $g(E)$ has a description depends on energy by the formula [44];

$$g(E) = \frac{4\pi(2m)^{\frac{3}{2}}}{h^3} \sqrt{E} dE \quad (3)$$

Kinetic energy formula can be utilized to find velocity depending equation;

$$E = \frac{1}{2}mv^2 \quad (4)$$

$$dE = mv dv \quad (5)$$

And the density of the state is obtained by using (4) and (5) as;

$$g(E) = \frac{8\pi m^3}{h^3} v^2 dv \quad (6)$$

The velocity should be considered in one direction. I assume the direction of the tunnel as x-direction. The velocity has components in all direction. However, I need the only x-axis component of the velocity. In other words, carriers that do not have x directional velocity do not affect the current in the x-direction. Therefore, the carriers should be distinguished regarding direction. In order to this, cartesian coordinates should change to spherical coordinates with those formulas;

$$dx = R \sin(\theta) d\phi, \quad dy = R d\theta, \quad dz = dr, \quad dx dy dz = R^2 \sin(\theta) d\phi d\theta dr \quad (7)$$

Where r, θ , and ϕ spherical coordinate components. After integration over sphere entirely with respect to ϕ and θ , the equation becomes;

$$dx dy dz = 4\pi R^2 dr \quad (8)$$

Similarly, the volume element containing in radial direction velocity is;

$$dv_x dv_y dv_z = 4\pi v_r^2 dv_r \quad (9)$$

v_x , v_y , and v_z are the components of the velocity in Cartesian coordinates and v_r is velocity in the radial direction. By substituting (9) to (6) the density state is ;

$$g(v) = \frac{2m^3}{h^3} dv_x dv_y dv_z \quad (10)$$

The components in y and z should be eliminated. The spherical coordinate transform formulas(7) are used, and I obtain term instead of v_y , and v_z ;

$$dv_y dv_z = v_r d\theta dv_r \quad (11)$$

By taking integral concerning θ and using kinetic energy formula the equation becomes;

$$dv_y dv_z = \frac{2\pi}{m} dE \quad (12)$$

and the density of state is;

$$g(v) = \frac{4m^2\pi}{h^3} dv_x dE \quad (13)$$

By using the formula (2) and putting (13) in it, the concentration of the carriers is;

$$n(v_x) = \frac{4m^2\pi}{h^3} \int f(E)dE \quad (14)$$

The current density is found as;

$$J_2 = \int_{v_x} qv_x \frac{4\pi m_2}{h^3} \int_E f_2(E)dE T(E_x) dv_x \quad (15)$$

Finally, by using equation (5), the current density formula from metal two to metal one is converted to;

$$J_2 = \frac{4\pi m_2 q}{h^3} \int_0^\infty T(E_x) \left[\int_E^\infty f_2(E)dE \right] dv_x \quad (16)$$

and similarly current density formula from metal one to metal two is;

$$J_1 = \frac{4\pi m_1 q}{h^3} \int_0^\infty T(E_x) \left[\int_E^\infty f_1(E)dE \right] dv_x \quad (17)$$

Total current density is

$$J(V) = J_2 - J_1 = \frac{4\pi m_2 q}{h^3} \int_0^\infty T(E_x) \left[\int_E^\infty f_2(E - V) - f_1(E)dE \right] dv_x \quad (18)$$

The total current density equation shows that the Fermi function is a factor that affects the total current. However, tunneling probability is the dominating factor for the total current density. In other words, the probability of electron tunneling preponderantly controls the current that occurs through the insulator layer sandwiched between metal one and metal two. Tunneling probability, $T(E_x)$, is a function of the potential barrier. There is no temperature dependence in the equation except Fermi distribution function.

The electron tunneling probability through insulator layer is defined with a well-known equation with Wentzel Kramers Brillouin (WKB) approximation as [41];

$$T(E_x) = e^{-2/\hbar \int_0^d \sqrt{2m^*(\Phi(x) - E_x)} dx} \quad (19)$$

Where d is the insulator thickness, m^* is the effective mass and $\Phi(x)$ is the potential barrier height between the the metal contact and the insulator layer. The tunneling probability formula indicates that the insulator layer's thickness effects the transmissions of the electron. The quantum tunneling current is calculated with Schrödinger Equations by solving with the Transfer Matrix Method (TMM)[45]. There are several decisive

parameters that the current depends such as barrier formation [46] and insulator thickness [45]. In other words, insulator layer thickness, bottom and top metal work functions and insulator layer affinity parameters should be considered to control quantum tunneling current[47]. The possible methods to enhance tunneling current are very thin insulator layer deposition such as few nanometers and low barrier height adjustment[48]. The barrier height is defined as the difference in metal work function and electron affinity of the insulator layer parameters. Moreover, asymmetric barrier formation provided by the top and bottom metal has a significant impact on tunneling current. The tunneling current could be improved by work function difference of the metals[49]. Also, when the bias voltage is applied to the structure, Fermi level of metal shifts [45] hence the work function of the metal is altered with respect to this shift and barrier height is changed. As a result, the tunneling current increases [50].

2.3. Photovoltaic Effect in MIM – Hot Electron

Photovoltaic effects in metals due to the photon excitation generates optical response [51]. Incident photon arrives on the surface of metal and couples to an electron that takes the energy to pass over upper energy states concerning photon energy. In MIM diodes, this excitation increases the tunneling probability because tunneling of the electrons at higher states is easy [7]. After MIM diode illumination, in the metal structures, hot electrons are generated. These hot electrons can pass the other metals either by tunneling through an insulator or over the barrier if the energy of the photons sufficiently larger than the barrier height [52]. The photoinduced hot electron mechanism has been investigated for Schottky barrier height [53].

Photon induced hot electron tunneling current is analyzed in three parts in which the incident photon energy is varied. I assume the barrier height between the metal one and the insulator layer, ϕ_1 is lower than the barrier height between metal two and insulator layer, ϕ_2 . The current density equation of the MIM diode driven in the previous section is converted to

$$J = \frac{4\pi m_2 q}{h^3} \int_0^{E_{\max}} T(E_x) \left[\int_E^{\infty} f_1^*(E) - f_2(E) dE \right] dE_x \quad (20)$$

where $f_1^*(E)$ is fermi function distribution of metal one under illumination condition and E_{\max} equals to $E_x + hf$. $f_1^*(E)$ is modulated on the Fermi energy level by the factor of

photon energy hf . If the distribution function is put into the equation, the equation is converted to

$$J = \frac{4\pi m_2 q}{h^3} \theta \left(\int_{E_F - hf}^{E_F + hf} T(E_x) (E_F + hf - E_x) dE_x - 2 \int_{E_F - hf}^{E_F + hf} T(E_x) (E_F - E_x) dE_x \right) \quad (21)$$

The equation should be evaluated in three-part such as $hf < \phi_1$, $\phi_1 < hf < \phi_2$ and $\phi_2 < hf$.

For $hf < \phi_1$, the current density can be found as [37];

$$J = \theta \frac{e \frac{m}{m^*}}{2\pi h d^2} (\phi_1 + \phi_2 - 2hf) e^{\frac{4\pi d m^* \frac{1}{2}}{h} (\phi_1 + \phi_2 - 2hf)^{\frac{1}{2}}} \quad (22)$$

where m^* is the effective mass.

For $\phi_1 < hf < \phi_2$, current density can be found as [37];

$$J = \theta \frac{(\phi_1 - \phi_2)^2 e \frac{m}{m^*}}{9\pi h d^2 (\phi_2 - 2hf)} (\phi_1 + \phi_2 - 2hf) e^{-\frac{4\pi d m^* \frac{1}{2}}{h(\phi_1 - \phi_2)} (\phi_2 - hf)^{\frac{3}{2}}} \quad (23)$$

For $\phi_2 < hf$, the current density can be found as [37];

$$J = \frac{4\pi m_2 q}{h^3} \theta \left(\int_{E_F - \phi_2}^{E_F + hf} (E_F + hf - E_x) dE_x \right) = \frac{2\pi m}{h^3} e \theta (hf - \phi_2)^2 \quad (24)$$

Equation (22) is the formula for Photon Induced Tunneling Current depends on Voltage, and the equation (24) is known as the Fowler relation for electron-photon emission. In the first case, there is only Photo-Induced Tunneling Current for hot electrons. In the second case, either diffusion or tunneling occurs. On the other hand, in the last case, there is only diffusion current because of photoemission of hot electrons [37].

3. Experimental MIM diode

In this chapter, design, fabrication, and characterization of MIM diodes studied for the content of this thesis is presented. I detail considerations during the structural design process, material selection, and band diagram, and then I explain the fabrication techniques that I pursued. I express characterization methods, setups and show my measurement results with the discussion.

3.1. Design of the MIM diode

The primary target of the project is to develop highly efficient MIM diodes for solar cell application. Thus, the design considerations focus on improving the performance of the devices. According to the current generation mechanism stated in the previous chapter, the insulator layer is the most decisive element in the structure for the performance; hence the investigation is predominantly headed to about the insulator layer.

Firstly, the insulator layer thickness is decided to be very thin in order to increase quantum tunneling. Also, the thin insulator layer decreases the internal resistance of the devices and increases responsivity because of an increase in current. By considering fabrication limitations, insulator thickness is arranged as around 1.5nm. However, the thin insulator layer results in a higher capacitive value. Insulator layer defines the active structure area. By keeping the active area in the range of μm^2 , the parasitic metal insulator metal capacitive effect is decreased to the femtoFarad range. To enhance the performance of the MIM diodes, the other factor that should be considered is nonlinearity that depends on the exponential relationship between tunneling current and tunneling distance. This relation is provided by asymmetry in the band diagram, the asymmetric behavior is maintained by material selection.

Design of the MIM diode is separated into two main sections. The first part is a single MIM diode and the second part is a different array format of MIM diodes.

3.1.1 Single MIM diode

Single MIM diode is designed to investigate the performance of different insulator layer and metal combinations. The active structure area defined by the insulator layer is $0.065 \mu\text{m}^2$. Along with decreasing parasitic effect, the small active area is intended to increase

the uniformity of insulator layer deposition, which is explained in the fabrication section. Figure 2 shows the design of the single structure

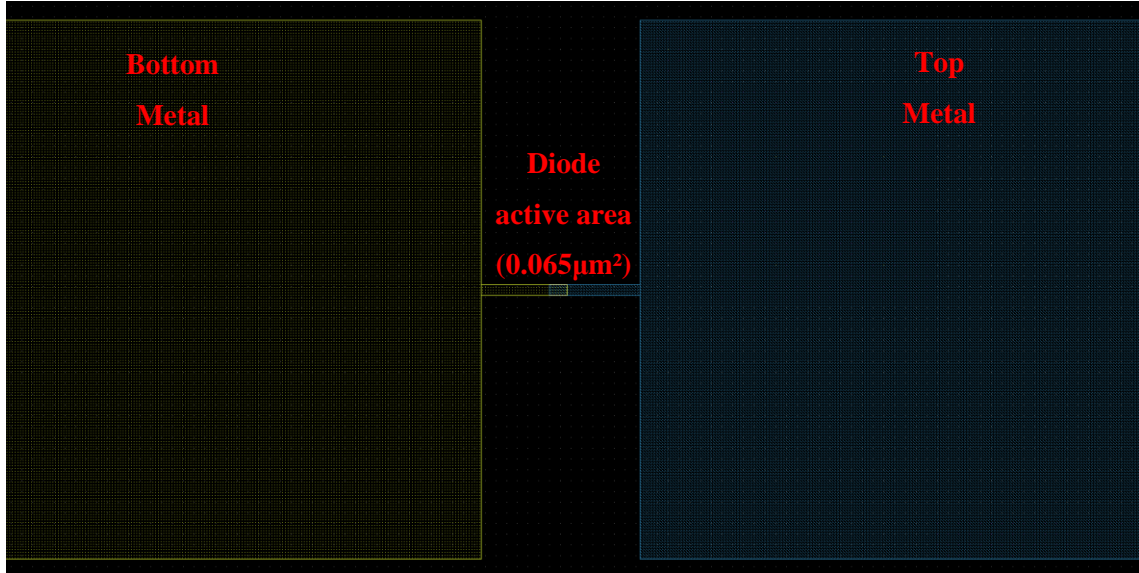


Figure 2 Design of a single MIM diode

The single MIM diode investigation is divided into two groups in terms of aimed observation factor. The first fabricated two devices are targeting to obtain outcome according to a comparison of two insulator layers on the performance of the devices in which the difference is induced because of the variation of the potential barrier height between metals and the insulator layer. Thus, to control this factor, metal layers are kept the same. The bottom metal for the devices is Au, and the top metal is Ni. The work function difference of these metals is low because we intend to obtain symmetric MIM diode. Thus, the factor of barrier height is isolated from the other effects. The work function of Au and Ni are 5.1eV and 5.15eV [54], respectively. Al₂O₃ and ZnO are implemented as insulator layers with electron affinity values 1 eV [55] and 2.08 eV [56], respectively. Al₂O₃ creates 4.15 eV barrier height with Ni while ZnO creates 3.07eV.

The second factor to observe is asymmetric barrier behavior. For this purpose, the bottom metal of the device is changed as Cr because the Cr work function is 4.5 eV [54] and it creates asymmetric barrier formation since top metal is Ni that corresponding work function is 5.15eV. Moreover, the insulator layer is decided as HfO₂, due to the fact that HfO₂ is a promising material for several applications, with its IC compatible and thermodynamic stable characteristics [50]. The electron affinity of HfO₂ is 1.75eV [57]. The MIM formation is leading to more asymmetric barrier formation at zero bias or non-

illumination conditions compared to first fabricated devices, as a result of Cr work function. The asymmetric barrier formation allows high quantum tunneling. The band diagram of each device shown in Figure 3. The dashed lines illustrate the barrier height modulation due to the light illumination.

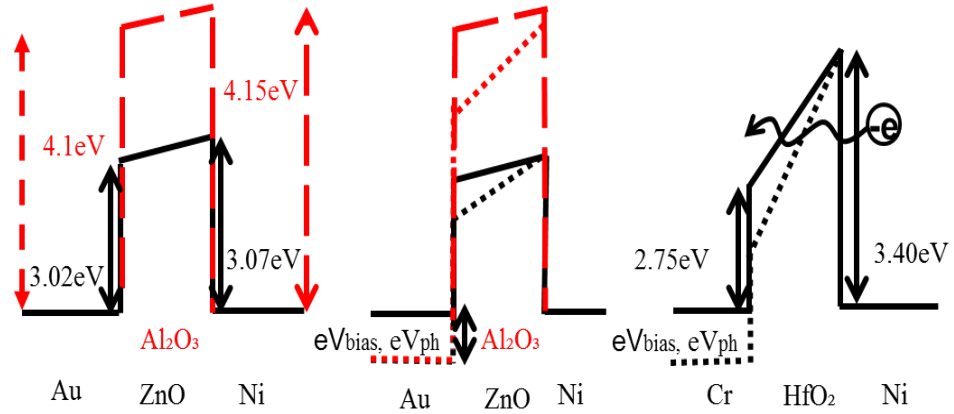


Figure 3 Conduction band diagram of an asymmetric barrier tunnel barrier with a barrier height of the MIM diodes

For electrons at higher energy levels, tunneling probability increases. The first diagram represents the equilibrium condition comparison of different insulator materials Al_2O_3 (red) and ZnO (black) with electron affinity values 1 eV and 2.08 eV, respectively as it is mentioned above. The work function of the Au and Ni are 5.1 eV and 5.15eV, respectively. The second figure shows the Fermi level shifting of the materials under applied dc bias voltage or light illumination condition represented by dotted lines for both Al_2O_3 and ZnO . The shift of the left side Fermi level is equal with the eV_{bias} or eV_{photon} where V_{photon} equals to $h\omega/e$. The last diagram is the symmetric barrier formation, barrier thickness and height tunability of the $\text{Cr}/\text{HfO}_2/\text{Ni}$ MIM structure with the change of applied DC bias voltage or light illumination condition. The work function of the Cr is 4.5 eV, and the electron affinity value of the HfO_2 is 1.75 eV as it is mentioned above. The barrier height between top metal, Ni and the insulators Al_2O_3 , ZnO and HfO_2 are 4.15eV, 3.07eV, and 3.40 eV respectively. All these material are selected to obtain an optical response in the visible range with corresponding barrier height.

3.1.2 Array Format of MIM diode

An array format of MIM diodes is implemented to observe improvement in performance of the device. In the format, MIM diodes are connected in parallel and 10x10 array is constructed. For this device, Cr/HfO₂/Ni material combination is used because the formation is expected to have more efficiency.

Interconnection lines for both the bottom and top metal are collected and connected to DC pads necessary for characterization. The line's width is 200nm to preserve line from fabrication defects. The interconnection lines are appropriately located with sufficient gaps in order to prevent parasitic capacitance formed through the substrate by metal lines. DC pad size is 100μm x 100μm. The design is presented in Figure 4.

3.1.3 Verification MIM diodes Optical Response

The devices have been fabricated on GaAs substrate. Although the GaAs wafer is highly resistive, the possible metal substrate junction formation should be considered. The junction contribution is purposed to investigate by fabricating devices without the active MIM area. Thus, all the effect of the other part of the structure is extracted. This investigation is the verification that the optical response is originated from the MIM diodes. The contribution of the metal semiconductor metal junction is evaluated with the design shown in Figure 5.

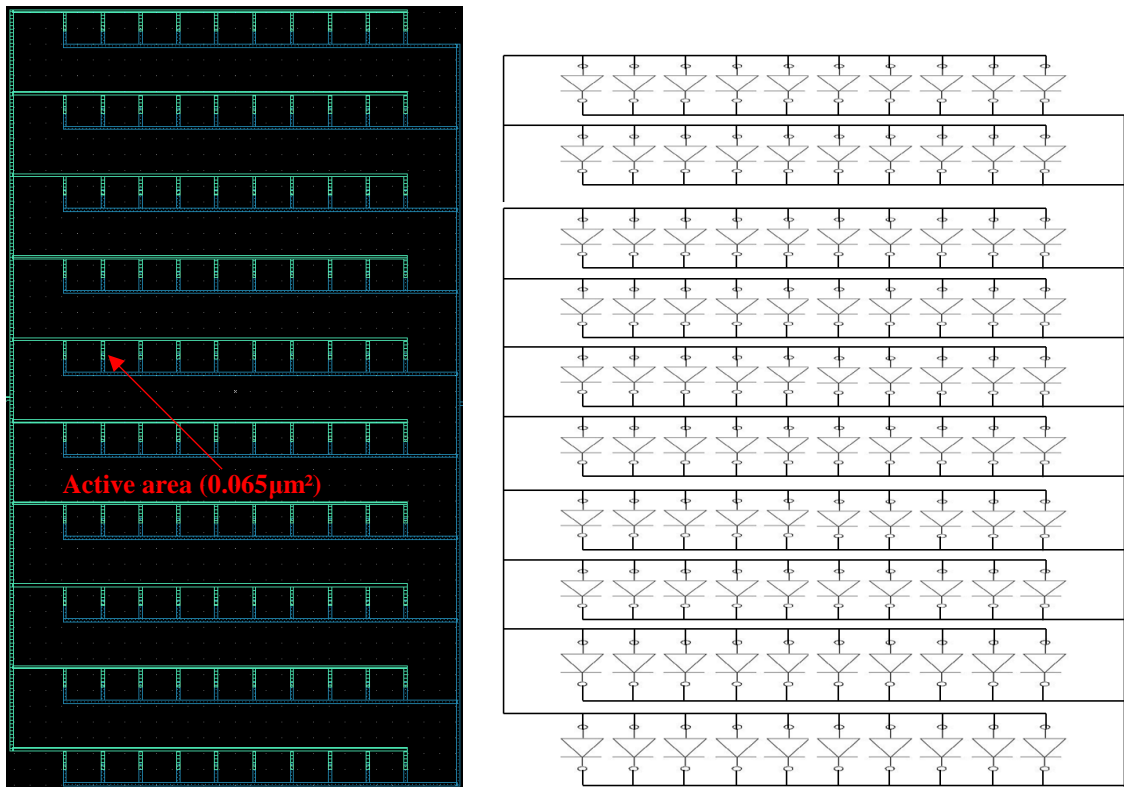


Figure 4 The layout and schematic of the 10x10 array

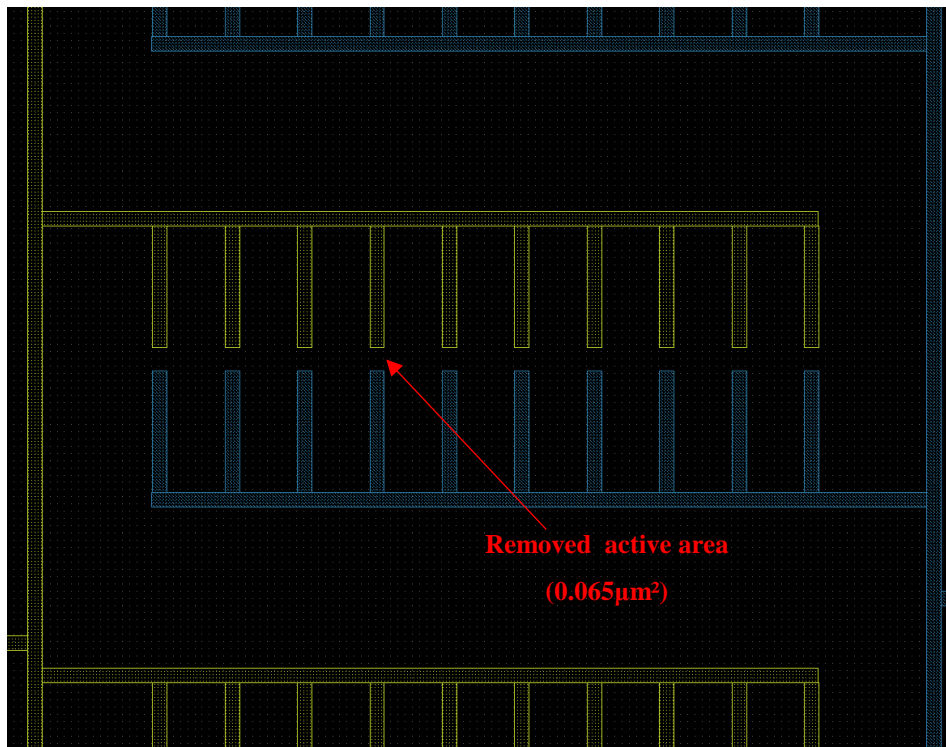


Figure 5 The design of the without MIM diode

3.2. Fabrication

The design and the barrier formations of the MIM diodes are made to collect incoming wave and convert to DC. The fabrication of the MIM diodes is performed in Sabanci University SUNUM facility. SUNUM facility has a capacity of nano-scale fabrication cleanroom equipment to obtain devices in nm^2 area. The most essential and used equipment to fabricate devices in nanometer size is Electron Beam Lithography (EBL). Physical Vapor Deposition (PVD) of the materials is done by using the Thermal and Electron Beam Deposition system.

MIM diodes are composed of three materials, which are metal-insulator-metal, and these three materials are fabricated step by step process as a stack. The devices are fabricated on top of a GaAs substrate, which is diced 1.5x1.5 cm pieces. The dicing process follows the substrate cleaning in order to coat the electron resist. The spin coating steps are used for electron resist polymethyl methacrylate (PMMA). The substrates are baked to stick the resist and also remove the moisture. After that, Electron Beam Lithography(EBL) is implemented to pattern nanoscale features. The resist is developed to achieve the open spaces for material deposition. Moreover, O_2 plasma cleaning is used to clean the residual PMMA from the developed open spaces. Although the O_2 cleaning step may thin the overall PMMA around 5 nm, the overall thickness of the resist compensates it. These steps are applied to each EBL process; then the substrate is ready for the material deposition. After material deposition, the lift-off process is performed. The material deposited substrate is put into a glass petri dish, and acetone (ACE) is poured over it. This process takes overnight. The substrate is cleaned with ACE and isopropanol (IPA) then dried with the N_2 purge. These steps are shown in Figure 6.

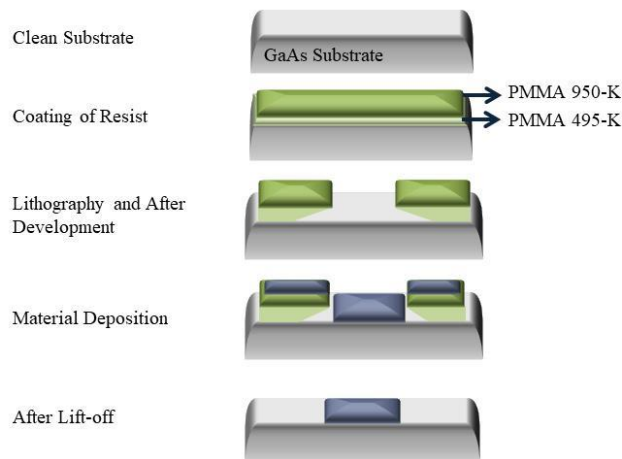


Figure 6 The representation of the fabrication steps in terms of material deposition.

The fabrication process starts with the substrate cleaning. Due to the dust, organic and inorganic residuals, the cleaning process is crucial to obtain high yield and quality fabrication. The substrates are cleaned by using AZ1165 remover in a glass petri dish and baked to 60 °C for 1 hour. Then the glass petri dish is put into an ultrasonic cleaner at 70% powers and 70 °C for 5 minutes. During the ultra-sonication process sample and glass petri dish collides hence the 100% of power did not use since GaAs substrates are fragile. The substrates are rinsed with acetone (ACE) and isopropanol (IPA) without drying ACE and IPA by itself. If they dry spontaneously, they leave stains on top of the substrate because the ACE and IPA molecules are heavy. Then the substrates are dried with the N₂ purge. As a final step of the cleaning process, substrates are cleaned by using O₂ plasma to remove residual of organic compounds. The O₂ plasma process is repeated every cleaning step and also developing process after EBL step. The substrates are examined by using a microscope to inspect that they are ready for the fabrication process. If they are clean, fabrication processes continue. Otherwise, the substrates go under same cleaning processes. After the cleaning process, the substrates are coated with PMMA and baked to ready for the EBL step.

3.2.1 Electron Beam Lithography

Electron Beam Lithography equipment is capable of patterning nm feature size. Since the MIM diodes are in nm size, this system is suitable for patterning the devices. To start the EBL process, firstly, substrates are needed to coat with the PMMA. PMMA is a positive resist for EBL, and high-resolution features can be obtained. The electron beam breaks the chemical structure of the PMMA, and it dissolves when the developing process is applied. The resists used in fabrication steps are 495-K and 950-K. To obtain the trapezoidal shape of the PMMA shown in Figure 6, 495-K PMMA and 950-K are coated, respectively. Because 495-K has low molecular weight, after electron beam exposure, it dissolves more than 950-K. Hence the trapezoidal shape is obtained.

The spin coating parameters are the same for both 495-K and 950-K PMMA. The first spin step has 100 Rsec², 1000 Rpm and is processed for 10 Seconds. The second spin step has 1000 Rsec², 5000 Rpm and is processed for 50 Seconds. The second spin step has 1000 Rsec², 0 Rpm and is processed for 5 Seconds. First, PMMA 495-K is spin coated and then baked at 175°C for 5 minutes. After baking, it is waited for cooling down the substrates to coat the second 950-K PMMA. The spinner and baking parameters are the

same for the 950-K PMMA. The PMMA thickness after two layers of coating and baking is around 300 nm.

The substrates are loaded to EBL holder and prepared for the lithography process. The MIM diodes are patterned with $500 \mu\text{C}/\text{cm}^2$ electron beam dose and 1.5 nA current. Because of the nm size of the MIM diodes, the low current level is selected to obtain high resolution. The pads are dosed with a higher current level around 20 nA. Moreover, the EBL equipment has a proximity effect correction option. This option leads that the features have exact sharp edges and are avoided overdose.

After EBL, substrates are developed with methyl-isobutyl-ketone (MIBK) solution. The development parameters of the features are 1:3 MIBK: IPA for 60 seconds, 1:1 MIBK: IPA for 5 seconds, and IPA for 60 seconds. Then samples are rinsed with IPA and dried with the N_2 purge. As a final step, samples are exposed to the O_2 plasma for the cleaning process of the residual PMMA on developed areas. O_2 plasma is taken for 5 seconds only. After the inspection of the samples with an optical microscope demonstrated in Figure 7, they are ready for the first metal deposition step.

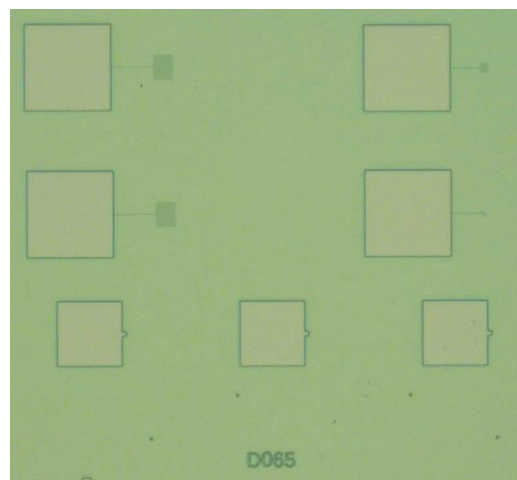


Figure 7 The optical microscope image of the structures after the first step of EBL and development.

3.2.2 Deposition of the Materials

The deposition technique that is used in fabrication is the PVD system. The metals are deposited in both thermal and electron beam deposition techniques.

The metal deposition with thermal evaporation is based on the melting point of the metals. Thermal boats are heated with the applied current and the material in the boats is firstly melted, and then evaporated. The thermal boats are made thermally durable to high temperatures. The evaporated material is deposited on top of the sample. However, some of the metals have too high melting points to deposit thermally. In this case, electron beam deposition technique is implemented. The electrons are emitted from the filament when the current is applied. The electrons are directed to the pot where the materials with magnets are located. Hence, electrons heat the material leading to evaporation. By using e-beam evaporation technique, it is possible to deposit metals having high melting points. The deposition rate is controlled with the filament current. The critical part of the deposition rate is to keep the ratio same and not to deposit at high rates to avoid metal stress on the substrate. In addition, the pressure in the chamber should be low in order to obtain clean, very low contaminated samples. The parameters used in deposition are given in Table 1.

Table 1 Metal Deposition Parameters

Material	Deposition Type	Pressure (Torr)	Current (A)	Rate (Å/s)	Thickness (nm)
Au	Thermal	8×10^{-6}	210	1	100
Ni	E-beam	7×10^{-7}	70×10^{-3}	0.7	70
Cr	E-beam	7×10^{-7}	50×10^{-3}	0.7	70
Ti	E-beam	7×10^{-7}	65×10^{-3}	0.5	3
Al	E-beam	7×10^{-7}	60×10^{-3}	0.7	70

3.2.3 Atomic Layer Deposition (ALD)

The insulator material is deposited with ALD equipment in Bilkent University. Depositing insulators with PVD system is very hard for few nm thicknesses. Hence, to obtain uniform, very thin insulator layers ALD equipment is crucial.

The main principle of ALD is to functionalize the surface with OH group. When H₂O vapor is absorbed by the surface, the OH group is formed. Then precursor gases react with the OH group and releases by-product. These by-product gases are pumped away. Hence one atomic layer is obtained basically. It is described as one cycle. Then again, H₂O vapor is sent into the chamber and forms OH group and precursor gases sent. This

process continues until the desired thickness is achieved. Hence, layer by layer growth deposition leading perfectly uniform insulator layer is obtained.

Atomic Layer Deposition precursor of HfO_2 is Tetrakis(dimethylamido)Hafnium ($\text{Hf}(\text{NMe}_2)_4$) fulfilled at 100°C , Trimethylaluminum (TMA) for Al_2O_3 and Diethylzinc (DEZ) for ZnO layers are growth at 80°C with H_2O precursors and N_2 as an inert gas. The low-temperature deposition is required due to the PMMA coating on the samples. Since PMMA break down at high temperatures is leading to an irregular shape and losing the trapezoid shape, low-temperature deposition is critical part of the fabrication process. The deposition rate of the materials for HfO_2 , Al_2O_3 and ZnO are 0.5, 1.35 and 1.25 $\text{\AA}/\text{cycle}$, respectively.

The lift-off process is applied to the samples after every deposition step. After the final lift-off process is completed, samples gain their final features. If the materials on top of samples are not cleaned from the lift-off process, the hot ACE technique is convenient to remove the materials from the undesired areas. ACE is heated up to $60\text{--}70^\circ\text{C}$ on a hot plate in a glass petri dish and samples are put in it and waited for around 30 minutes. However, the ratio of the PMMA and the deposited material should be 3:1 to have clean lift-off process. Also, ultrasonic cleaning can be applied at low power not to damage the features. The SEM images of the final shape of the samples are shown in Figure 8.

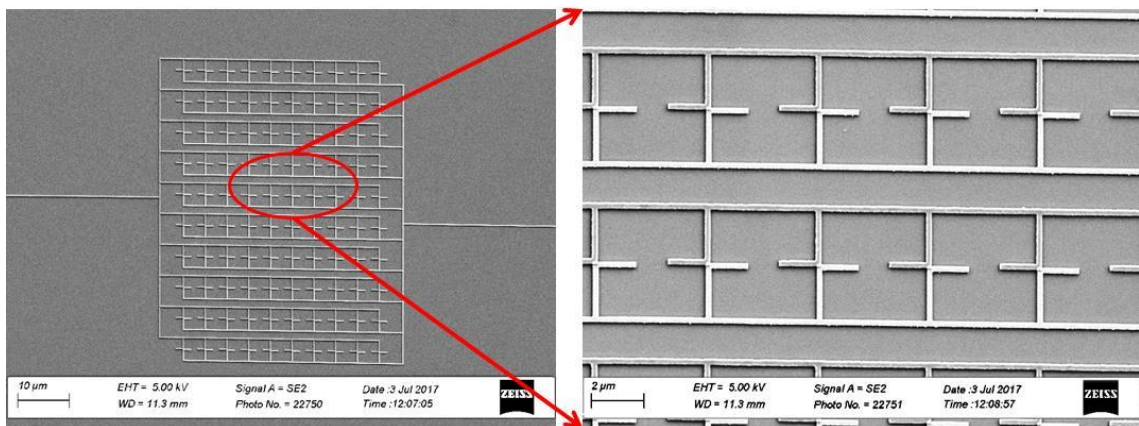


Figure 8 SEM image of the MIM diode

3.2.4 Mask Layouts

The EBL uses mask files that are generated by the layout editor programs so that it directly patterns the features on top of the samples. Unlike the optical lithography equipment, there is no mask to shadow the samples and obtain the features.

There are three mask sets used in the study. The first is given in Figure 9. The mask is generated for Cr/HfO₂/Ni samples. The overall composition of the structure is is. The samples are fabricated as both single and 10x10 array formats.

The second mask set is given in Figure 10. The mask is identical for Au/Al₂O₃/Ni and Au/ZnO/Ni samples. The active area of the samples is the same in Cr/HfO₂/Ni as 0.065 μm².

The third mask set is drawn by removing the MIM diodes active areas. The purpose of the fabricating samples without MIM active area is to investigate the metal substrate junction effects and to determine the origin of the optical response of the structures whether coming from the non-MIM diode or the MIM diode itself. The mask is shown in Figure 11.

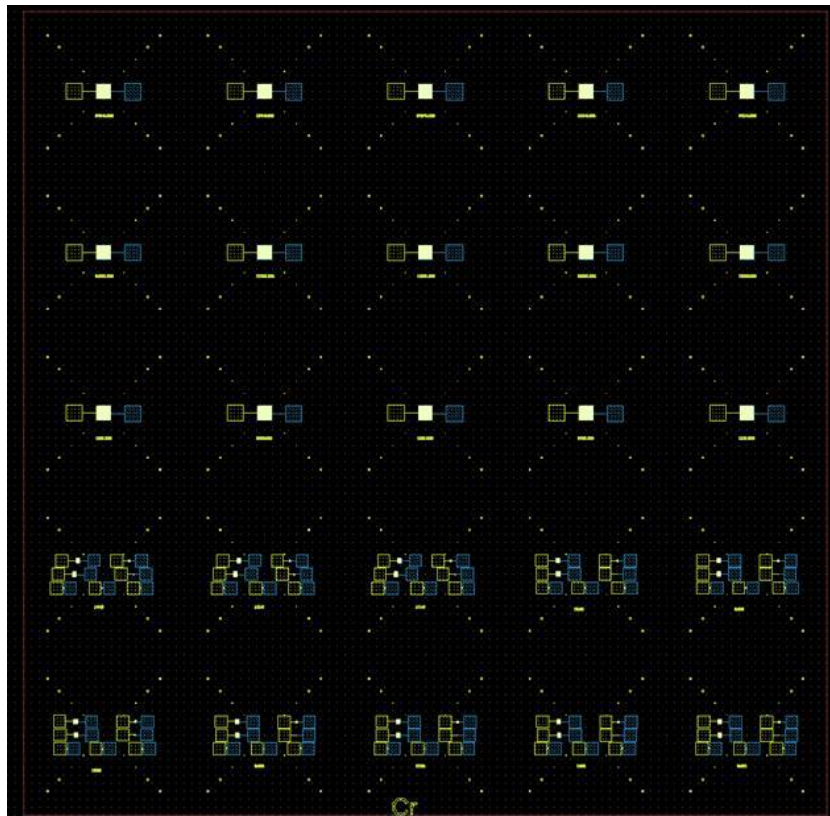


Figure 9 The mask for Cr/HfO₂/Ni samples

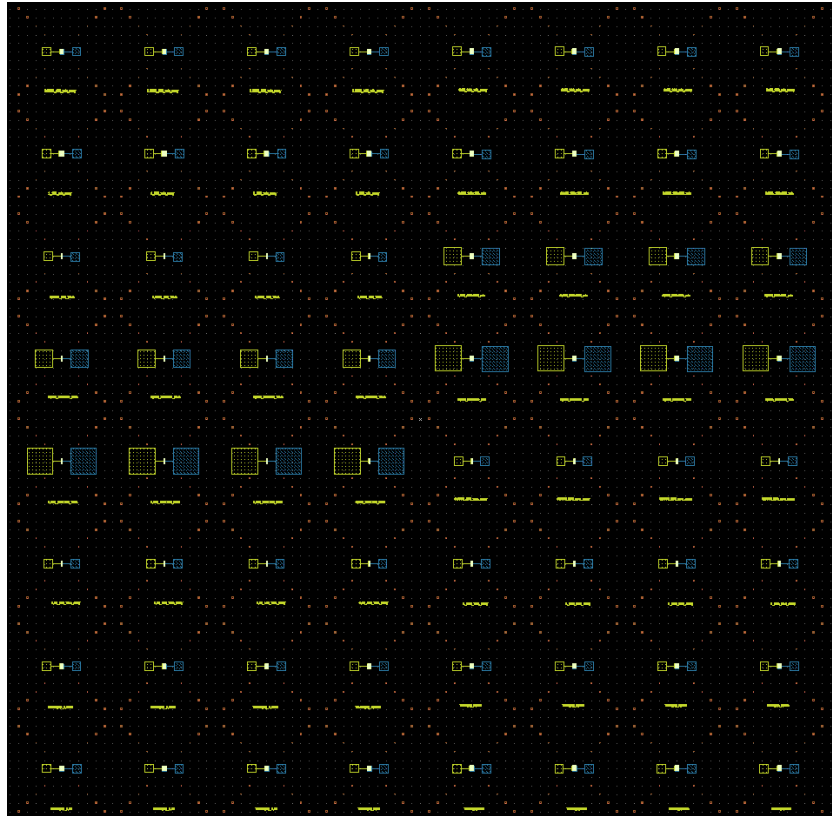


Figure 10 The mask for Au/Al₂O₃/Ni and Au/ZnO/Ni samples

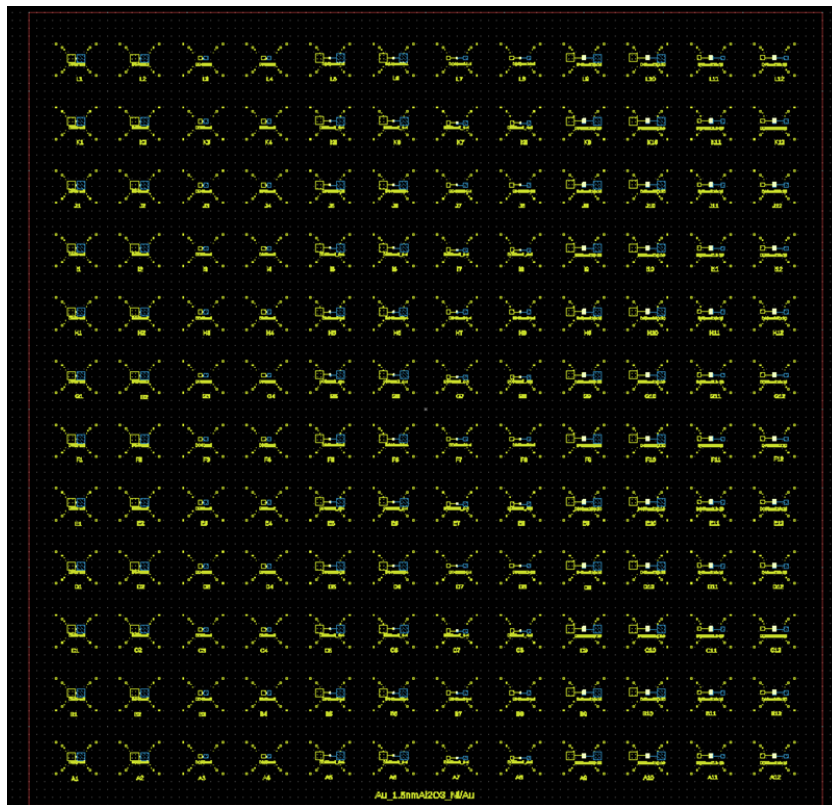


Figure 11 The mask for without MIM diode

3.3. Characterization

In this part of the thesis, I explain characterization methods in detail, and I show the results. Characterization of the devices is separated in terms of content and purpose. The devices are firstly physically characterized in order to detect the quality of fabricated devices. After that, the devices are electrically characterized to determine the performance. Moreover, the optical response of the devices is tested during the electrical characterization.

3.3.1 Physical Characterization

Physical Characterization of the devices is carried out to detect fabrication defect, material existence and quality of the fabrication process. During the fabrication process, the samples are examined with the inspection method. Fundamentally, optical microscope detection is the primary inspection. Beside after material deposition process, the thickness is inspected with KLA-TENCOR P6 Surface Profiler whether the material is deposited with a predetermined thickness.

After fabrication, several physical characterization methods are implemented to the devices. The first method is to examine the devices with Energy Dispersive X-ray Spectroscopy (EDX). EDX working principle is based on the fundamentals that each element has own electromagnetic spectrum. It is used to investigate material existence. Figure 12 demonstrates EDX spectroscopy results.

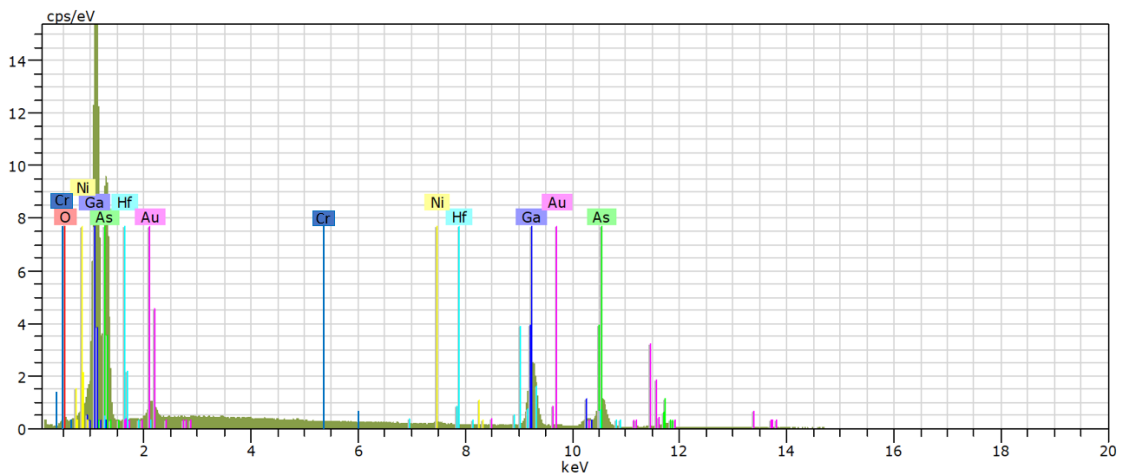


Figure 12 EDX Spectroscopy results of the Cr/HfO₂/Ni structure

The other method that I used in characterization is Ellipsometry Analysis. Ellipsometry is used to measure optical characteristics of thin films such as reflection, transmission,

refractive index, etc. Moreover, by using Fresnel equations, the system can calculate the thickness of the material. The detection mechanism is to investigate polarization change while the radiation interacts with the material. I used Ellipsometry Analysis to investigate absorption of the devices concerning incoming radiation's wavelength. The light source emits radiation to the devices with an incident angle by focusing spot on centering. The radiation reflects over the sample and is collected by the detector. The detector calculates the reflection from the power of collected radiation.

Ellipsometry Analysis result of the Cr/HfO₂/Ni single MIM diode on GaAs substrate mentioned in section 3.1.1 is illustrated in Figure 13. The result is the average of the s and p polarization. It shows that MIM diode absorption has a peak value in the visible and the Near IR range. Furthermore, the absorption of the bare GaAs substrate is added to indicate that the selective optical absorption results of the MIM structure are originated from the devices. There is no transmitted light detected; all the incident light is either reflected and detected by a detector or absorbed. The absorption is extracted from reflectance obtained from the Ellipsometry Analysis. Furthermore, there is also an embedded Ellipsometry tool to the ALD system. The tool is purposed to determine the thickness of the deposited material. Hence, the insulator deposition thickness is controlled during the ALD process.

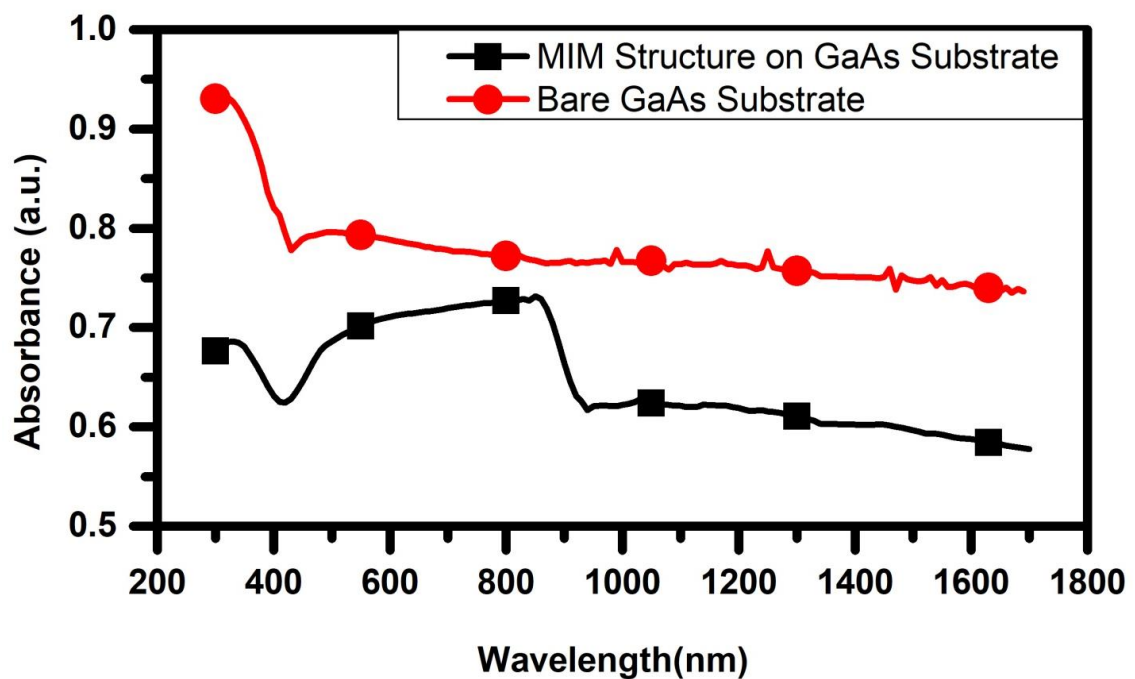


Figure 13 The ellipsometry results of the MIM diodes and bare GaAs substrate

3.3.2 Electrical Characterization

I performed DC characterizations of the MIM diodes by using Agilent B1500A Semiconductor Parameter Analyzer. The Semiconductor Parameter Analyzer consists of Source/Measure Units (SMU), Windows embedded control system, custom design Kelvin Contact for 4 point probe sensing. A Source/Measure Unit is a module to source and measures voltage current at the same time. In other words, it is a voltage/current source and a voltage/current meter. Therefore, the analyzer is capable of providing I-V measurements.

The measurements are taken by applying DC bias voltage to DC pads of the devices via mechanically controlled DC probes, in a dark environment, generated in the shielded probe station. The probe station is grounded to avoid noise signal to deteriorate the measurement by coupling. Also, the shielded probe station provides dark environment by block the light with its non-transparent surface. The DC characterization setup is shown in Figure 14.

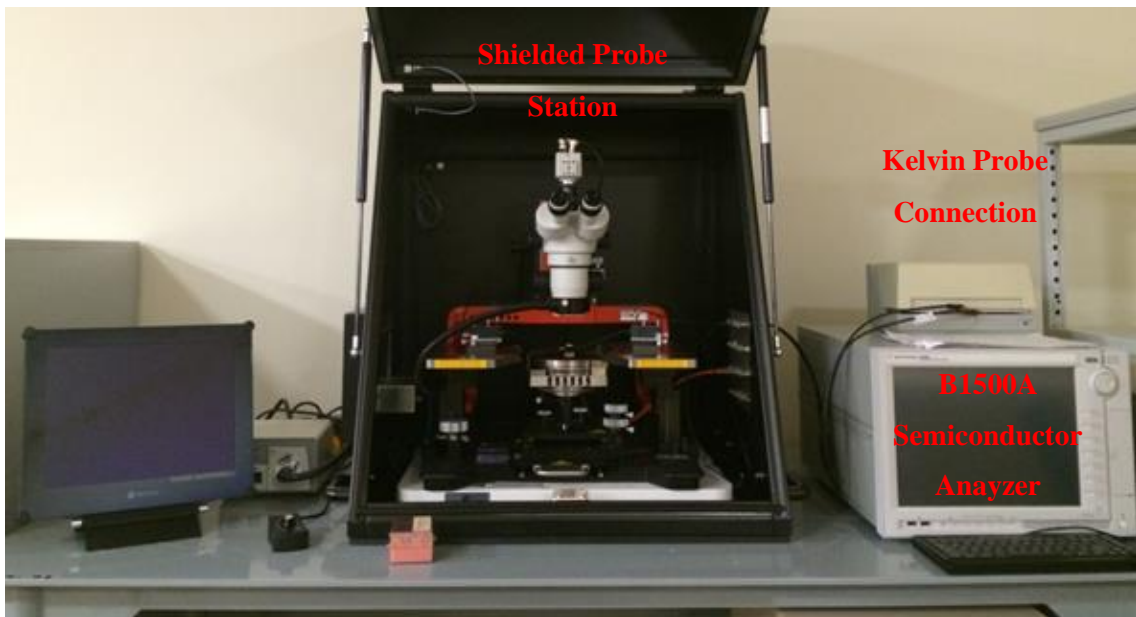


Figure 14 DC characterization setup

A halogen lamp, Motic 150C, like a visible light source, with controlled intensity, is placed inside the probe station in order to investigate the effect of the optical radiation on the current level. The power of the halogen lamp is measured by an optical power meter, Newport Dual Channel Power Meter 2832-C. The optical intensity on the surface of the

chamber that the samples are located is $6\text{mW}/\text{cm}^2$. The spectrum of the halogen lamp is measured and shown in Figure 15.

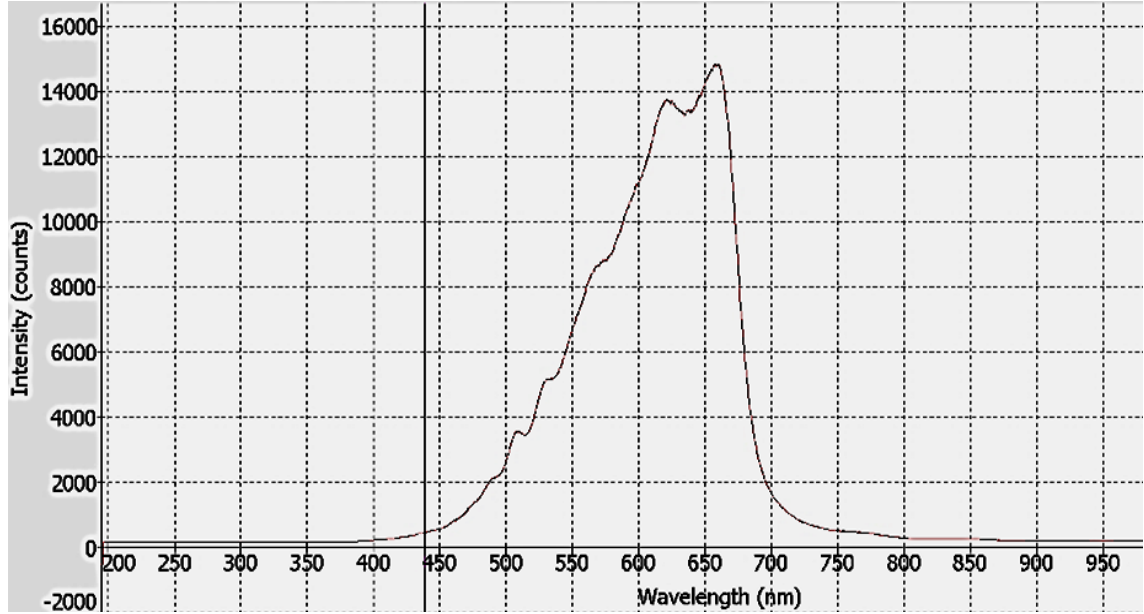


Figure 15 The spectrum of the halogen lamp

The results show that the optical radiation emitted from halogen lamp includes wide range wavelength between 400-900nm. Also, the peak wavelength is around 650nm.

The DC characterizations contain extraction of I-V characteristics with respect to incident light intensity. The responsivity of the devices denoted (S) is extracted from the I-V characteristics. The parameters needed to calculate responsivity, are resistance (R) and nonlinearity, and they are extracted using equations (25), (26) and (27).

$$R = \frac{dV}{dI} \quad (25)$$

$$\text{Nonlinearity} = I'' = \frac{d^2I}{dV^2} \quad (26)$$

$$S = \frac{1}{2} RI'' = \frac{d^2I/dV^2}{2dI/dV} \quad (27)$$

3.3.2.1 Measurement Results of Single MIM diodes

The I-V characteristics of the three different devices; Au/Al₂O₃/Ni, Au/ZnO/Ni and Cr/HfO₂/Ni are measured for the first part of the DC characterization. The visible light is applied to measure the response of the devices. The intensity of the visible light source is tuned in two variations such as half of the maximum intensity, $3\text{mW}/\text{cm}^2$ and maximum

intensity of the source, $6\text{mW}/\text{cm}^2$. The response of the devices to the illumination source is observed through a change of current levels.

The responsivity values of the devices are extracted from the I(V) characteristics, taken under illumination of the visible light with 100% intensity, by using equation (3).

Figure 16 and Figure 17 are the I-V characteristics of Au/Al₂O₃/Ni and Au/ZnO/Ni respectively. The first investigation is about comparing insulator in a symmetric MIM diode. As a result of the high barrier height between the metal and the insulator layer for Au/Al₂O₃/Ni, the structure has low quantum tunneling current in the dark situation. The dark current level of Au/ZnO/Ni is considerably high, at the 400nA level. However, Au/Al₂O₃/Ni has more increment regarding current, under the visible light. As it is mentioned in chapter 2, the reason is that high barrier height between the metal and the insulator contribute to more tunneling distance modulation with respect to Fermi level modulation that occurs during illumination, in comparison to low barrier height shown in Figure 3. The maximum current of the Au/Al₂O₃/Ni is 800nA under visible light illumination. The responsivity values of the Au/Al₂O₃/Ni and Au/ZnO/Ni are 1.68 A/W and 0.84 A/W, respectively, at zero bias condition.

The second investigation is about asymmetric barrier formation. In the Cr/HfO₂/Ni structure, work function difference of the metals generates more asymmetric barrier formation leading to more barrier height modulation under illumination. Figure 18 presents the I-V characteristic of Cr/HfO₂/Ni structure under visible light illumination. Figure 19 is the responsivity of the three structures under visible light illumination. As it is expected, Cr/HfO₂/Ni structures result in higher responsivity as a result of asymmetric barrier formation. The maximum current of the Cr/HfO₂/Ni is 800nA under visible light illumination. The responsivity of Cr/HfO₂/Ni structure is 1.75 A/W at zero bias condition.

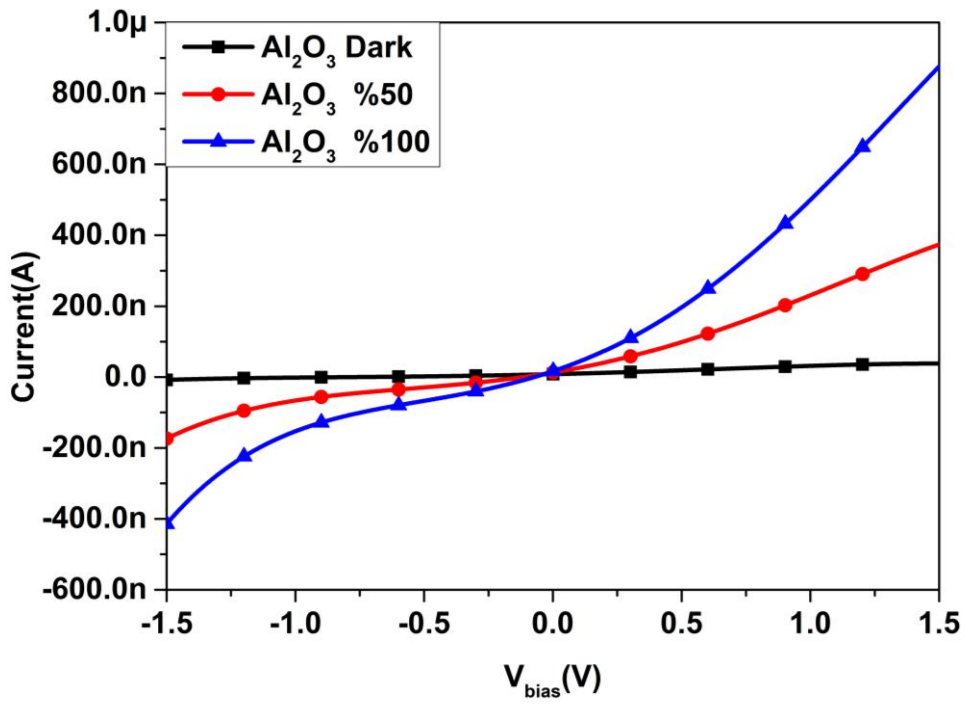


Figure 16 I-V characteristic of Au/Al₂O₃/Ni with respect to the illumination

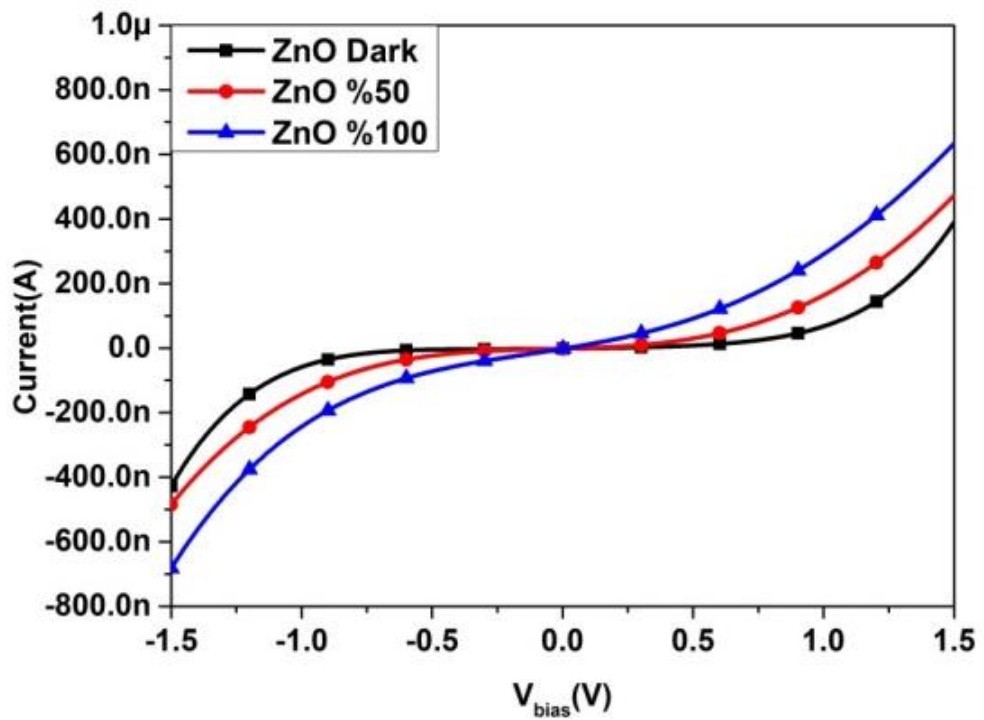


Figure 17 I-V characteristic of Au/ZnO/Ni with respect to the illumination

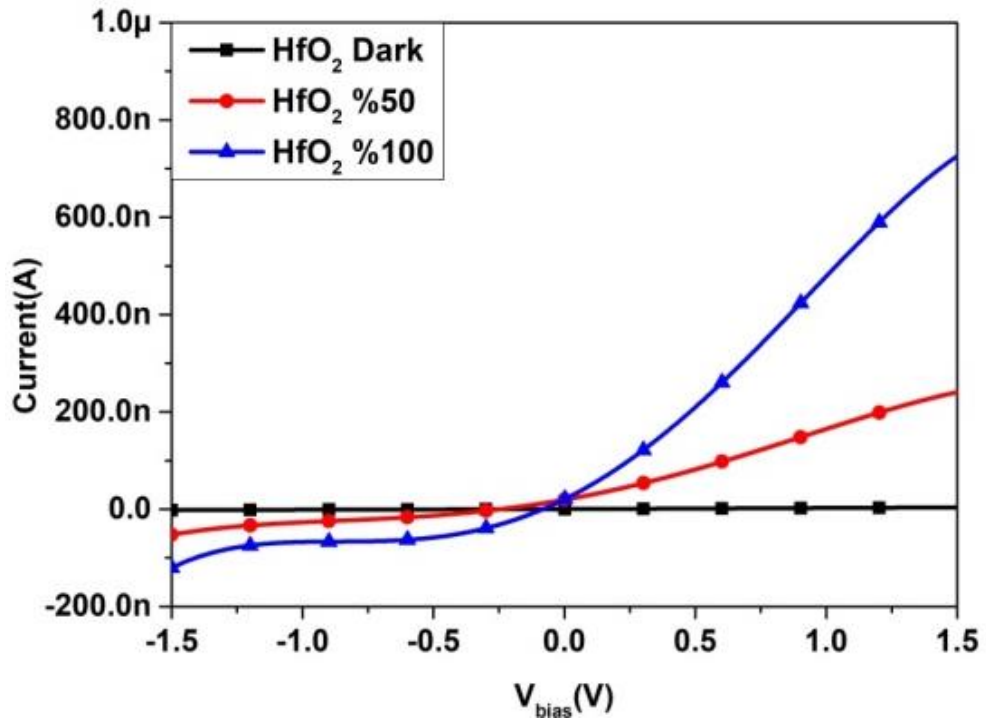


Figure 18 I-V characteristic of Cr/HfO₂/Ni with respect to the illumination

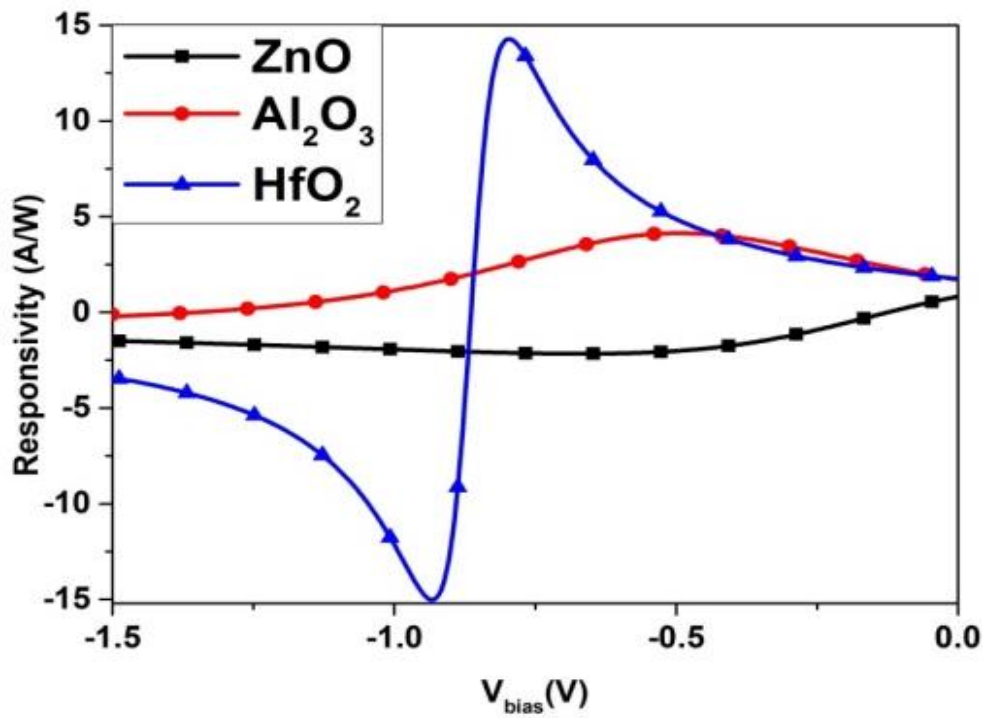


Figure 19 The responsivity of the structures with respect to the insulator layer

3.3.2.2 Measurement Results of 10x10 Array MIM diodes

The potential improvement on the performance of the MIM diode leads further investigation for an array implementation that is mentioned in the design section. The 10x10 array construction is performed with the material selection of Cr/HfO₂/Ni structure that is expected to have high responsivity due to the asymmetric barrier formation. All the devices are connected in parallel mentioned in detail in section 3.1.2.

DC characterization of the devices is carried out with taking I-V characteristics by the increasing radiation intensity of the halogen lamp step by step. shown in Figure 20. Similar to single structures, the current level of the structure with applied bias has increasing behavior concerning optical radiation. The current change concerning different optical intensity is illustrated in Figure 21. As it can be seen from the graph, more bias voltage allow more variation in current under the same amount of optical radiation. The forward bias response is larger than the reverse bias response as it is expected because of the large tunneling distance seen from the barrier height in Figure 3. Thus, reverse bias has a smaller change under illumination compared to forward bias.

The other observation is fulfilled by current- time sampling with a constant bias voltage. For this observation, I gave constant 1V bias with 100ms time interval for a long period. The results are presented in Figure 22. The characterization targets to observe the repeatability and reliability of the optical response. After 500 second dark condition with applied 1V, the intensity of the light is changed to 25%. The current is stabilized instantaneously with exceptional noise. This short time reaction indicates the fast response of the MIM diodes. Then 1000th second, the illumination is shut down. The current falls to the previous dark condition level. 50%, 75%, and 100% intensity tests are carried out with the same method, with 500 seconds periods. All dark currents are in the same range, and the increment in the current with respect to intensity is logically proportional. The test shows that the MIM diode has a repeatable optical response. The reason for the noise is investigated after the experiment. Although the samples are located in a shielded cage mentioned before, the microscope camera that exists in order to control the probe connection to DC pads propagates 50 Hz AC signal originated from electrical lines, and the AC signal is coupled to the probes. I explain the method of how to eliminate this noise signal in the next section. In Figure 22, the current level is smoothed by a step function with average values in order to clarify step by step optical response of the structure.

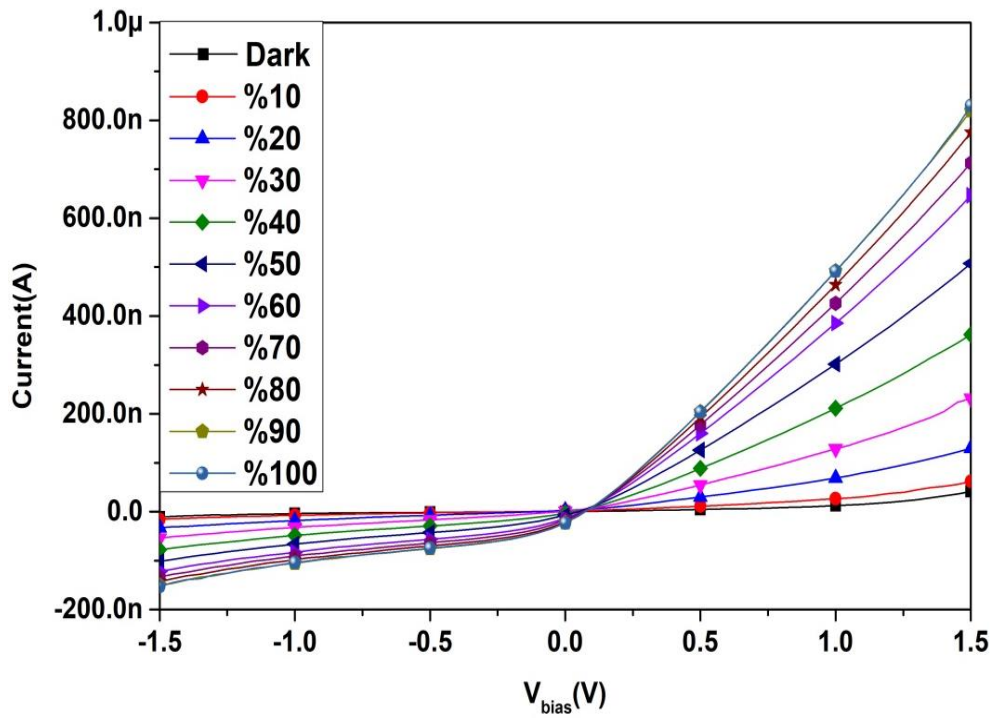


Figure 20 I-V characteristic of 10x10 array with respect to optical intensity

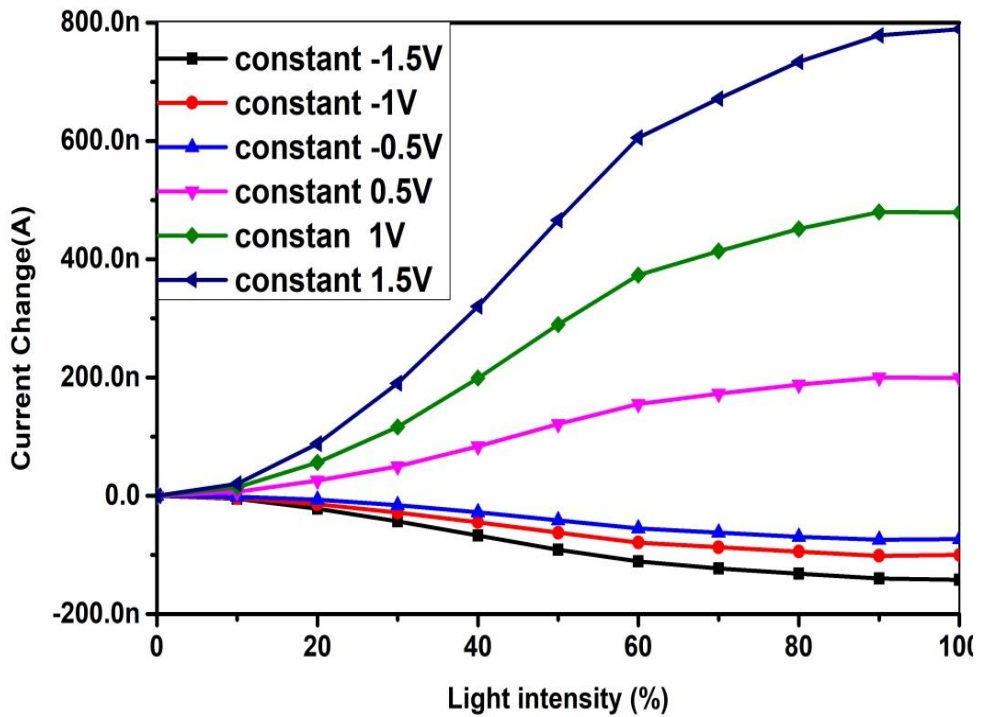


Figure 21 Current change vs. Optical intensity with respect to different bias voltages

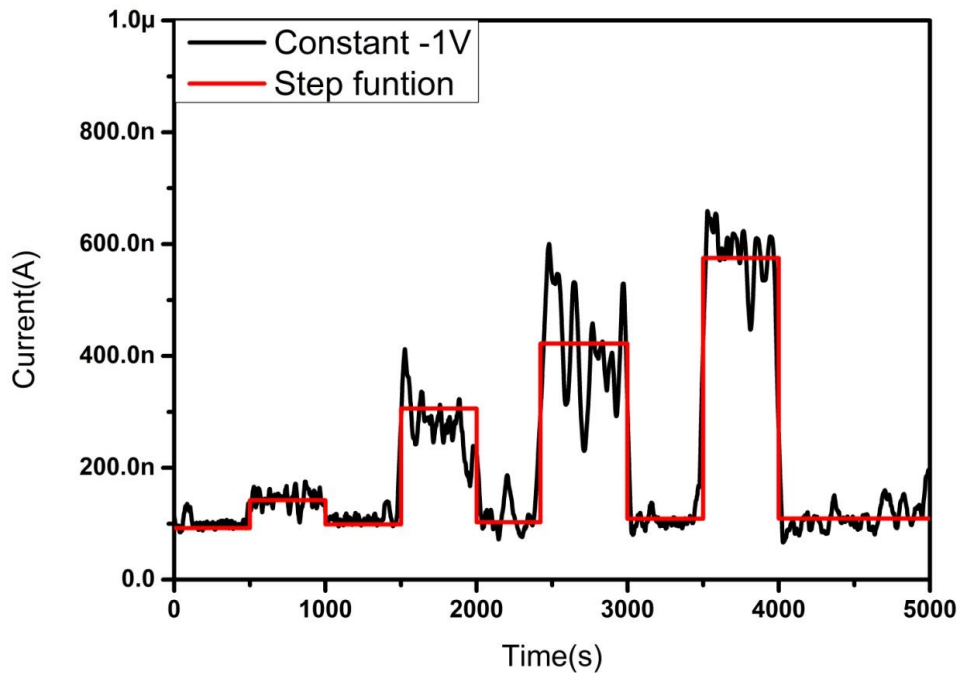


Figure 22 I-t sampling at constant 1V in order to show repeatability

3.3.2.3 Measurement Results of Verification MIM diodes Optical Response

The investigation of possible undesired metal-substrate-metal junction formation is performed with an additional prototype design mentioned in the 3.1.3 section. The junction may contribute optical response of the MIM diode, due to the optical characteristic of GaAs semiconductor substrate. For this purpose, the active area of the MIM diode is removed all the remaining parts are kept same.

The test of the without MIM structures was practiced under the same optical condition. The results of the without MIM diodes are presented in Figure 23. The dark current of the device is in pA level while the current under illumination reaches only a few nA levels. Figure 24 presents the comparison of without MIM diode and MIM diode regarding the optical response. It can be commented that without MIM diodes has a contribution to optical response. However, it is negligible when it is compared to the MIM diode. Therefore, this is the verification that the optical response is predominantly originated from the MIM diode.

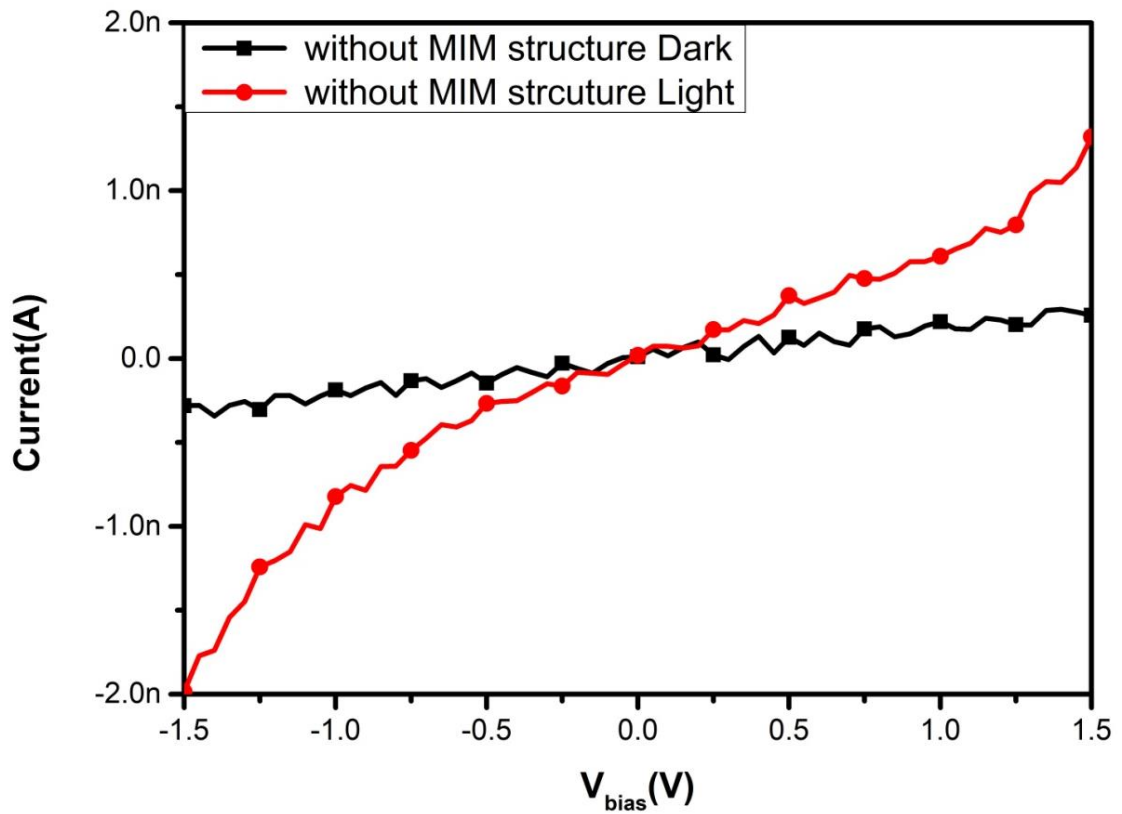


Figure 23 I-V characteristics of without insulator layer with respect to optical radiation

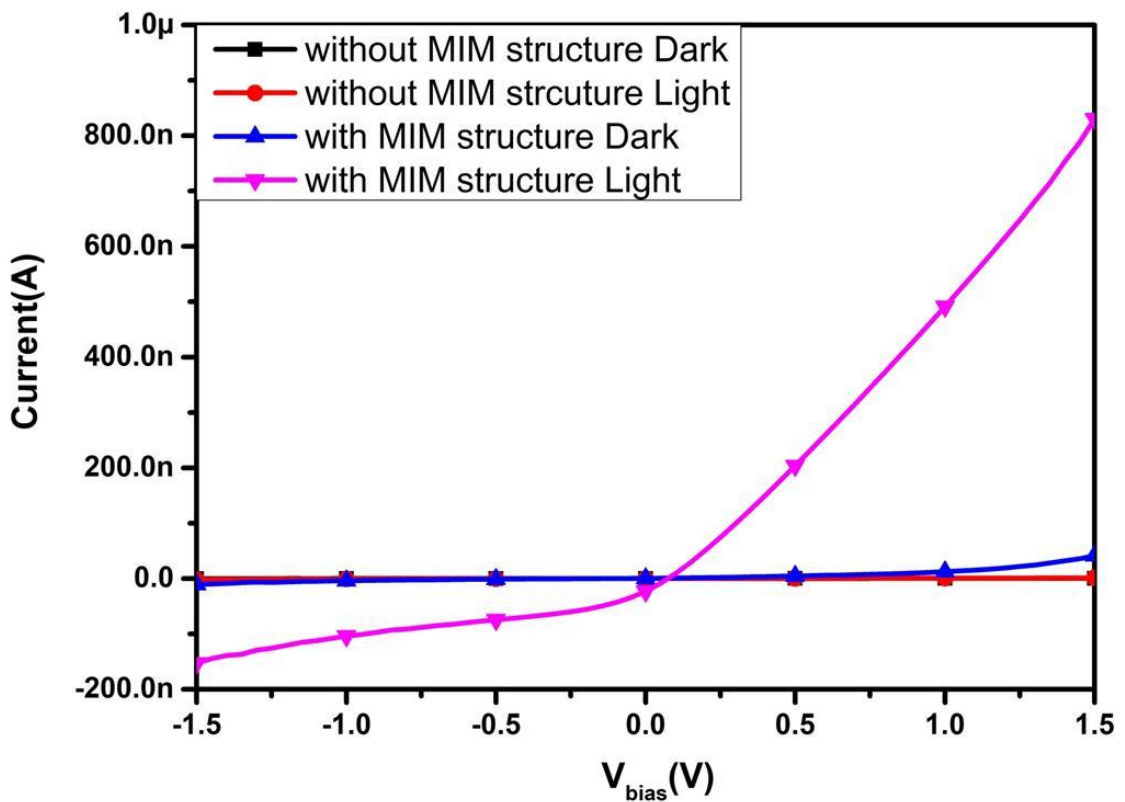


Figure 24 The comparison of the without MIM diode and MIM diode

3.4. Efficiency Calculation

Efficiency is generally described as the ratio output power to consumed input power. In this study, a description of the efficiency has been modified to the ratio of the output electrical DC power generated by the MIM diode to incident optical radiation power. In other words, it corresponds to optical power consumption to generate such electrical DC power due to the photovoltaic effect in the structure.

Calculating efficiency is a challenge since extracting output power in the nanoscale device is difficult. Also, the input power should be isolated as only optical power remaining factor responsible for generating current. Therefore, voltage bias should not be applied during the measurement. Furthermore, to obtain external output power by measurement, the photon generated current as result of photon-induced tunneling should be transferred to a load. Integration of the load resistance to the nanoscaled fabricated device is the main challenging factor for the calculation. The formulas to calculate efficiency are;

$$\eta = \frac{P_{\text{Output}}}{P_{\text{Input}}} = \frac{P_{\text{Output}}^{\text{DC}}}{P_{\text{Optical}}} \quad (28)$$

$$\eta = \frac{P_{\text{Output}}^{\text{DC}}}{\text{Incident Radiation Intensity} \times \text{Collector Area}} \quad (29)$$

A custom design isolated load box has been used during the output electrical power. The MIM diode modeled as a current source connected to the internal resistance of the structure. The load resistance shares photon generated current with internal resistance. Maximum power transfer method is considered for the design. I calculated electrical output power from the DC voltage across the load resistance. Figure 25 is the circuit diagram of the measurement setup. The load resistance is isolated from the environment with a box that surface is grounded. The transfer of the current is carried out with isolated cables and BNC connectors. Figure 26 shows the load box and the resistive load. Since the internal resistance of the MIM diodes is different, the constant load resistance is connected in order to compare the optical performance of the devices.

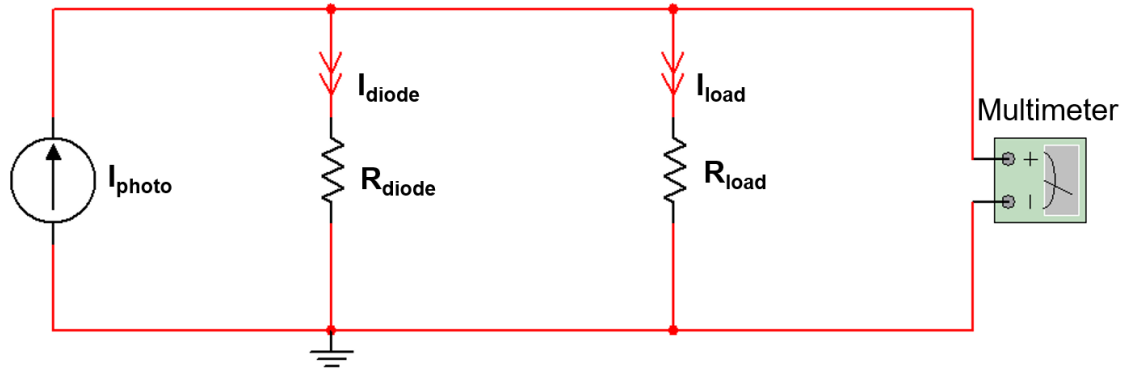


Figure 25 Circuit diagram of the measurement setup

Obtained efficiency values are not the maximum values due to a small mismatch between load and the internal resistance. Different insulator layers in the structures cause the difference among the internal resistance. However, the range of the internal resistance of the structures is less than $10\text{M}\Omega$ for all single structure. Thus, the load resistor is selected as $5\text{M}\Omega$.

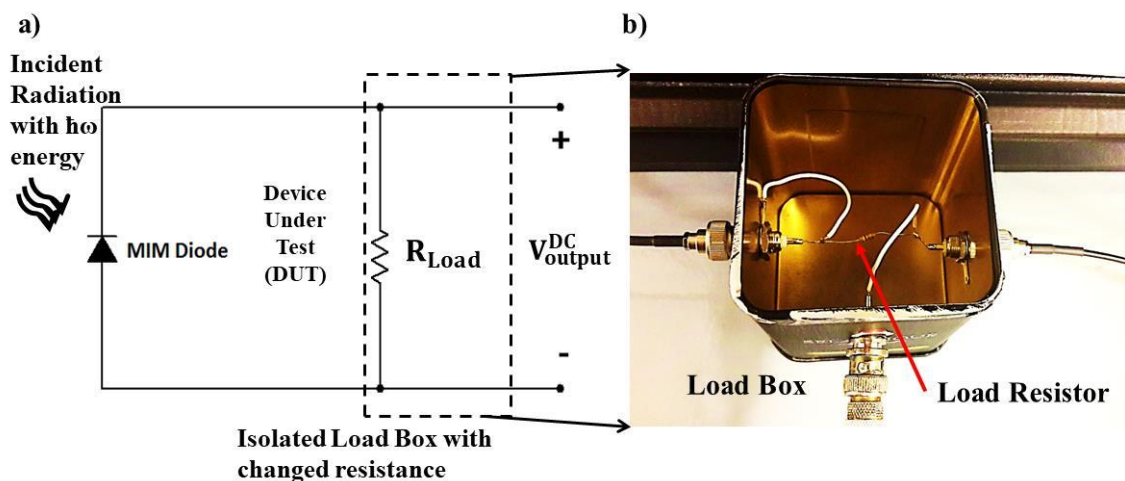


Figure 26 Isolated load box in order to obtain output power from MIM diode

Furthermore, I have already measured the incident optical intensity with Newport Dual Channel Power Meter 2832-C for DC characterizations. The maximum intensity is $6\text{mW}/\text{cm}^2$. I assume the collector area as the directly the active area for single MIM diodes. On the other hand, the active area is multiplied with 100 for 10×10 array format calculations. The gap between the samples and the light source is 8cm. However, the measured intensity value is obtained on the surface of the chamber that the samples located. The light source is randomly polarized.

Efficiency calculation results of the single MIM diodes are in the table. The parameters used during the calculation are also presented in the table. According to results, Cr/HfO₂/Ni is the most efficient structure, as it is expected from the DC characterization and responsivity results. The higher value is attributed to asymmetric barrier formation of the structure, hence the high quantum probability.

Table 2 Efficiency Measurement Results for Single MIM diode

MIM Formation	Active Area (μm ²)	Element Number	Load Resistance (MΩ)	Voltage Across Load Resistance (mV)	Output Electrical Power (pW)	Input Optical Radiation Intensity (mW/cm ²)	Efficiency (%)	Responsivity (A/W)
Au/Al ₂ O ₃ /Ni	0.065	Single	5	1.8	0.648	6	16	1.68
Au/ZnO/Ni	0.065	Single	5	1.5	0.45	6	11	0.84
Cr/HfO ₂ /Ni	0.065	Single	5	1.9	0.72	6	18	1.75

The output electrical power level is around one pW while the consumed electrical power is 3.9 pW. The voltage across the 5MΩ load reaches 1.9mV for Cr/HfO₂/Ni single MIM diodes. It can be emphasized that the structures have occupied less than 1 μm².

The efficiency of the 10x10 array of the MIM diode formed by using the single Cr/HfO₂/Ni is presented in Table 3. The measurement is extended by adding another light source, 625nm wavelength LED. The optical power intensity of the LED is 4 mW/cm² and the gap between the sample and the LED is 2 cm. The efficiency measurement setup is shown in Figure 27.

The output electrical power level is not comparable for state of the art solar cells. However, the obtained output power from μm² range area is an achievement and direct our studies to evaluate the efficiency in terms of the conversion of the optical power consumption. In other words, the efficiency of the devices is evaluated as the ratio of useful electrical output power to consumed optical power. This method is different than the conventional solar cell efficiency calculation because array optimization is not performed in order to obtain comparable data. On the other hand, 10x10 array results provide promising output power for further improvements.

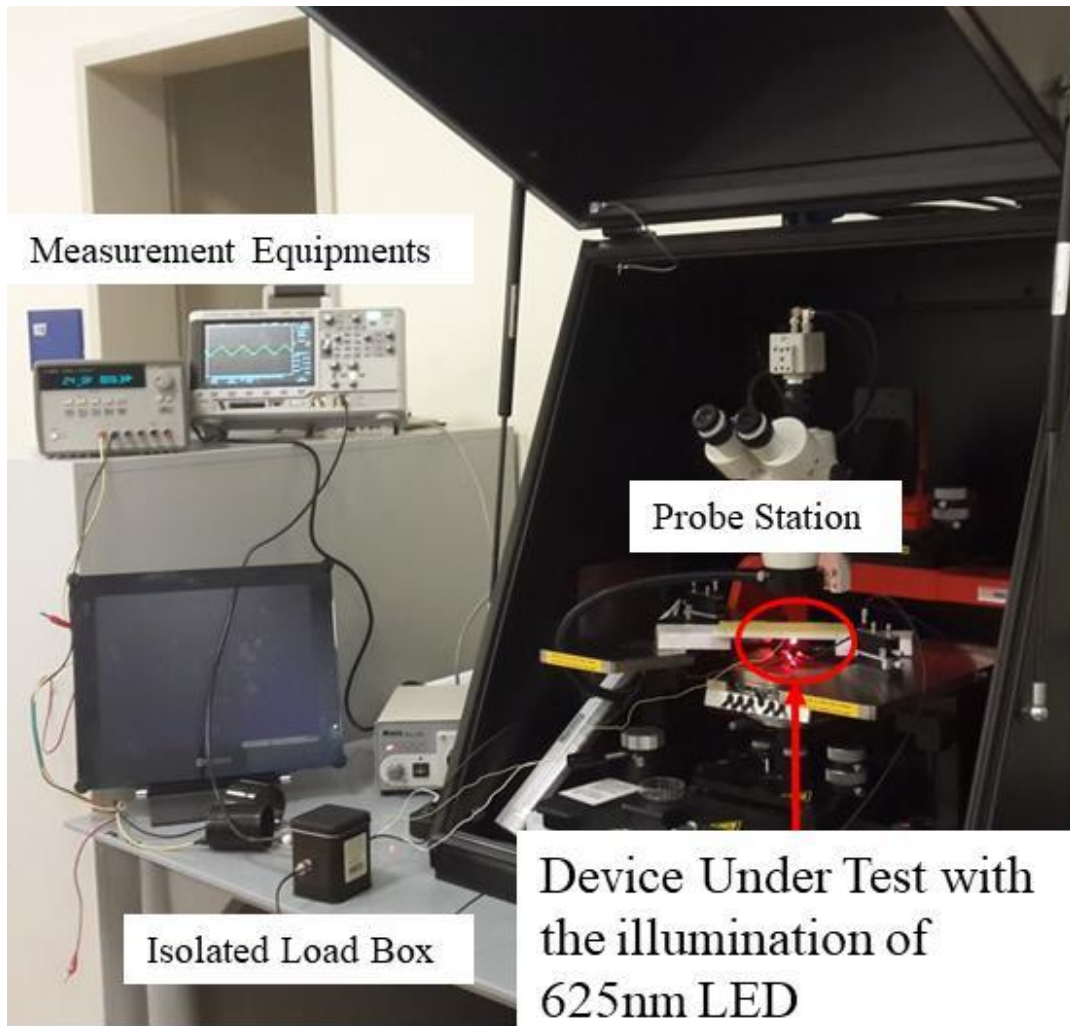


Figure 27 Efficiency measurement setup with the illumination of 625 nm LED

The results show that the efficiency of the array is considerably high in comparison to a single structure. The efficiency increases from 18% for the single diode to 29% for array structure. The efficiency is improved by forming an array as it is expected. The output power rises to 115.2pW as the consumed optical power is 390pW. The voltage across the load resistance is 24 mV. Moreover, I obtained an optical response to 625nm wavelength red LED. The efficiency value for the LED is 12%.

Table 3 Efficiency Measurement Results for 10x10 MIM diode

Illumination Source	Voltage Across 5 MΩ Load Resistance (mV)	Output Power (pW)	Incident Radiation Flux (mW/cm ²)	Efficiency (%)
Visible Light	24	115.2	6	29
625 nm LED	12.7	32.2	4	12

I evaluated the efficiency values with a constant load. The reason for measurement with constant load is that the resistance of all structures is different and to obtain comparable data, I needed to fix the load resistance. On the other hand, to examine maximum power and the efficiency value, maximum power transfer method is applied by changing constant load resistance with variable resistance to find exact matching between load and the internal resistance. For $3\text{M}\Omega$ load resistance, the efficiency has reached 30% as it is shown in Figure 28. The result indicates that the internal resistance of the structure is around $3\text{M}\Omega$.

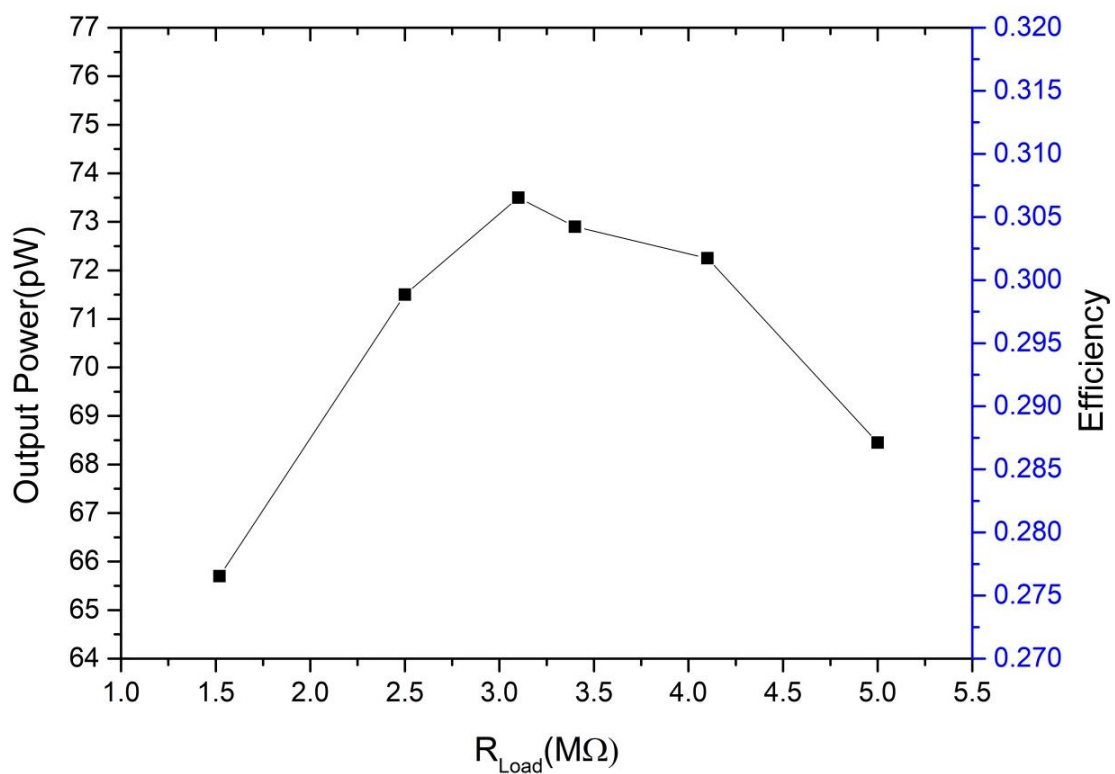


Figure 28 Variable R_{load} test to find maximum power transfer

During the measurement, I discovered that there was a coupled AC signal to DC probes from the electrical line. The signal deteriorated the DC level at the output. In order to acquire reliable results, the measurement setup is advanced. A custom design measurement setup that consists of instrumentation amplifier supplied with batteries and a low pass filter that cutoff frequency is 7 Hz has been constituted. Moreover, differential input between the cathode and the anode is successfully converted to the single-ended voltage input.

The operation of the measurement setup can be clarified that photon generated current from the MIM diode is transferred to $5M\Omega$, resistance pair to obtain differential input voltage. 9V battery supplies the instrumentation amplifier to boost the differential input voltage with fixed ten gain through $5.6K\Omega$; the boosted single-ended voltage output is filtered by RC low pass filter in order to eliminate noise because of coupling AC, and finally the output voltage is measured with a multimeter. All these operation are performed inside the shielded load box. Furthermore, to eliminate possible noise caused by battery, 100 nF shunt capacitors are connected to positive and the negative supply input nodes. The filter is composed of 100 k Ω and 220 nF capacitors and has 7 Hz cutoff frequency. The coupled AC signal from electrical line has 50 Hz frequency, and with this filter, it is eliminated. The circuit diagram of the setup is presented in Figure 29 The efficiency of the 10x10 array rises from 29% to 40% as the output voltage reaches 30 mV for the halogen lamp test as it is illustrated in Figure 30. Similarly, efficiency of the array for 625nm LED test increases to 20% as it is shown in Figure 31.

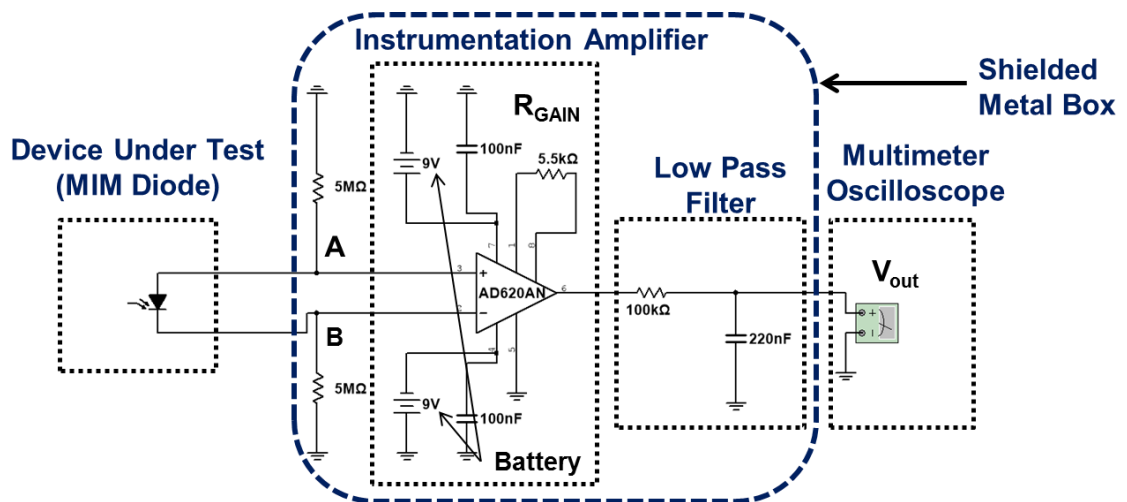


Figure 29 The circuit diagram of the low noise instrumentation amplifier design for efficiency calculation

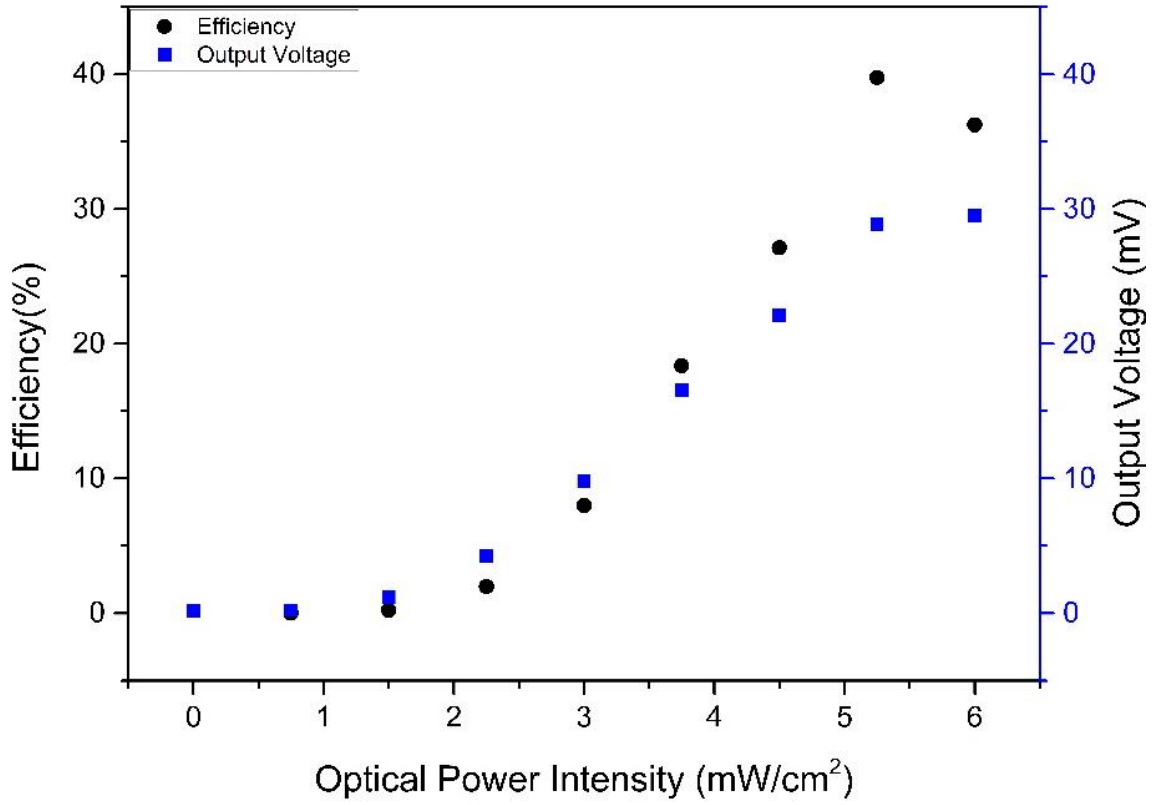


Figure 30 Efficiency measurement with advanced setup for Halogen Lamp

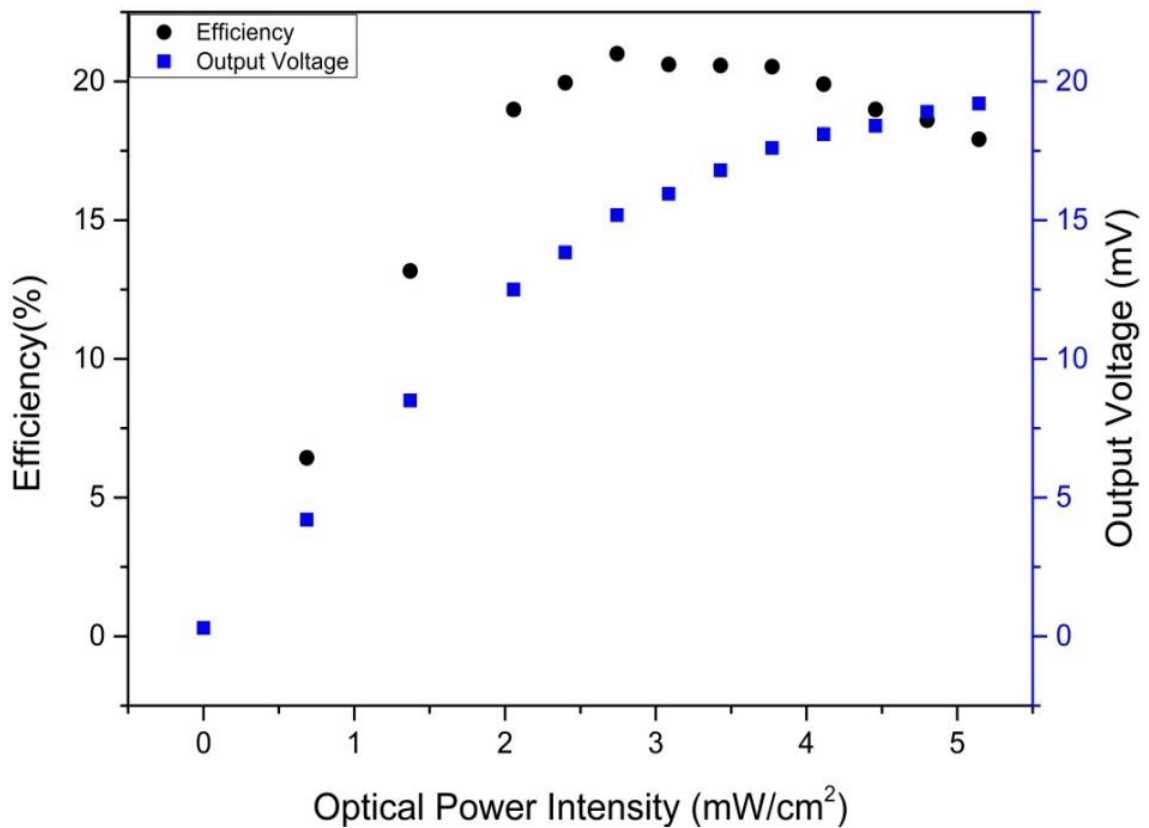


Figure 31 Efficiency measurement with advanced setup for 625 nm LED

4. Stand Alone Converter Evaluation Module Design

In the previous chapter, the optical response of the MIM diodes is demonstrated by firstly DC characterizations in the form of I-V curves and then by efficiency calculation measurement setup generated predicating on maximum power transfer method. On the other hand, up to this chapter, the output of the MIM diode based solar cell is evaluated on a resistive load that consumes the harvested electrical power by the solar cell. Nevertheless, the demonstration is intended to extend by designing a stand-alone evaluation module that takes the output of the MIM diode as an input to convert it to useful electrical power for charging the rechargeable battery or a capacitor. The module is a good impression of a MIM energy harvester.

The converter module contains low power, self-biased power manager integrated circuit. LTC 3108 is selected since the input voltage requirement is indicated as 20 mv by using a DC-DC step-up converter with a transformer to boost the output of the solar cell before the integrated circuit. The output of the integrated circuit can be programmed to a fixed voltage suitable to charge the rechargeable Lithium battery. Figure 32 is a diagram of the working principle of the module.

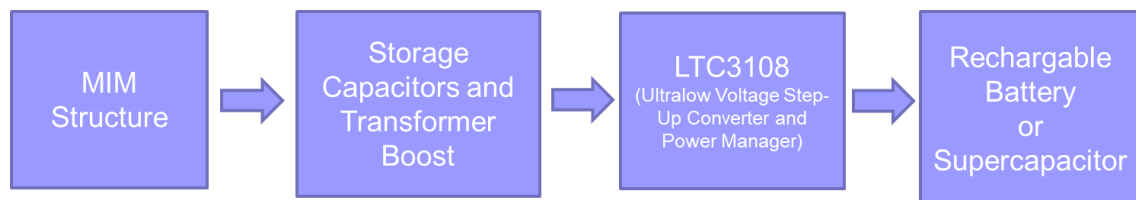


Figure 32 Working chain of the converter module

4.1. Operation of Ultra Low power Step up Converter

LTC 3108 from Analog Device, Linear Technolgy is an integrated converter for DC to DC applications and an ideal component for harvesting, low input voltage sources such as thermoelectric generators, thermophiles, and small solar cells. It operates form inputs of 20 mV by using a compact step-up transformer circuitry. It has selectable output voltage as 2.35V, 3.3V, 4.1V, or 5V. The output has logic control and reserve energy storage. The proposed applications are remote sensors and radio power, surplus heat energy harvesting HVAC systems, industrial wireless sensing, automatic metering, building automation and predictive maintenance. It has two packaging options, thermally enhanced 12-lead DFN package and a 16-lead SSOP package.

Operation of the integrated circuit starts with an oscillator that consists of switch MOSFET to create a step-up oscillator. It is needed to operate with a 20 mV minimum input voltage. The purpose of using an oscillator is to boost the input voltage to regulate output voltages. The oscillator should be coupled with an external transformer to complete the boosting process. The oscillator creates AC voltage at the end of the transformer, this AC voltage is rectified in an integrated circuit and generates current to output pins for charging external capacitors.

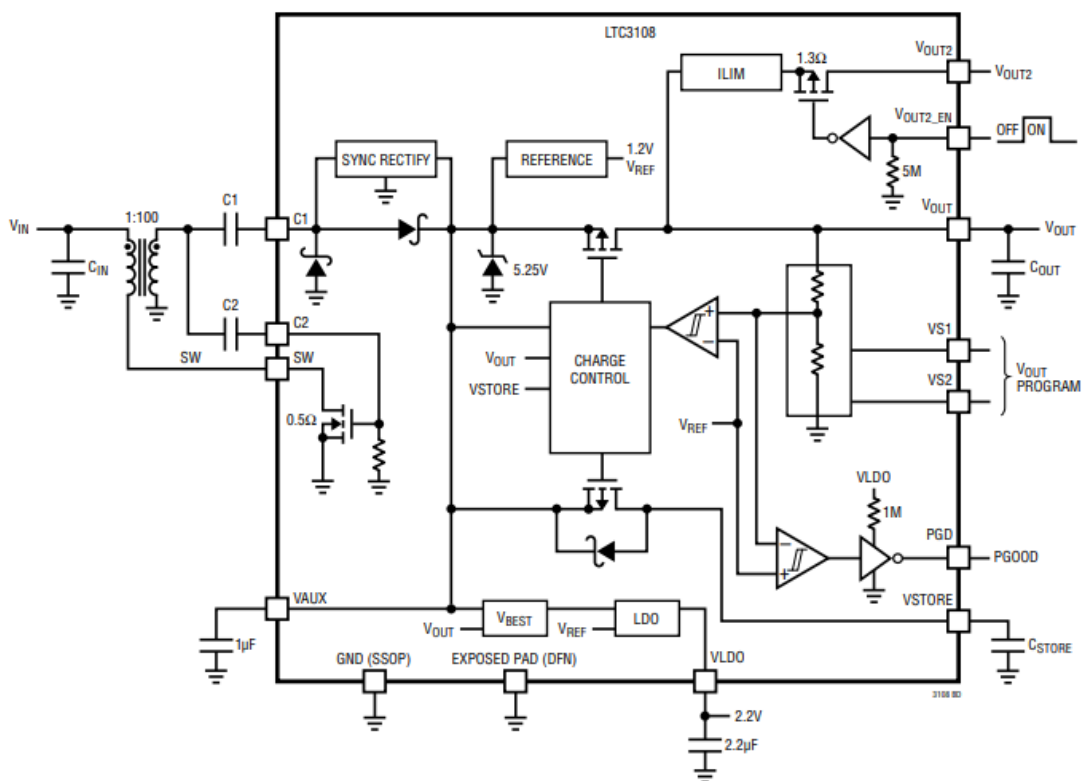


Figure 33 Block diagram of the LTC 3108 [58]

There are several outputs of the LTC 3108. VAUX is the first output that is activated by the current of the rectifier. VAUX has two assignments, the first assignment is to supply the active circuits and the second is to program the output voltage connected battery to charge. Also, after VAUX reaches 2.5V, Low Dropout Linear Regulator starts to be activated and has 2.2 constant voltage to supply low power processors and integrated circuits. The 2.2µF ceramic capacitor is needed for stability of the Low Dropout Output. Moreover, the VAUX begins to charge Vout. The maximum value of the VAUX is 5.2V by regulator limiter if the input source provides more power than requirements. Furthermore, there is also another output pin charged by VAUX, VSTORE. The purpose

of this pin is to charge V_{out} when the input source is unable to provide current unintentionally. The block diagram of the LTC 3108 is presented in Figure 33 [58].

4.2. Design

The Design of the converter module is carried out with KiCAD program. Firstly, the step-up converter is formed. To obtain an output with 20mV input, the winding ratio of the transformer should be 1:100. The transformer works with the oscillator in the LTC 3108. The primary winding of the transformer is connected a switch MOSFET, which creates an oscillation at the end of the secondary winding. The resonant frequency is determined by the secondary winding inductance and the load capacitance connected to the C_2 pin. LPR 6235 transformer is selected, and the primary winding inductance is 7.5 μ H. To keep oscillation resonant frequency in the range of 10 kHz and 100 kHz which is recommended by the company [58], the C_2 capacitor is selected as 330pF. With the value of 330pF load capacitance and 75mH secondary winding inductance, the resonant frequency is around 30 kHz that satisfies the requirement. The charge pump capacitor takes a role in arranging converter input resistance and maximum output current capability. If the source resistance is high and the source voltage is low, the capacitor value should be minimum 1 nF. The squegging effect that may cause burst in the oscillation is avoided by connecting a bleeder resistor, 499k Ω , in parallel with C_2 capacitor. The C_{out} and C_{store} capacitors are selected by considering the current limitation recommendation of the company as 220 μ F [58].

Figure 34 is the schematic of the converter module design. After schematic design, the layout of the design is drawn with the program to fabricate module on Printed Circuit Board(PCB). The layout is shown in Figure 35. The Layout Versus Schematic (LVS) is checked. Then, the 3 D model of the design is generated. The frontside and the backside of the model are shown in Figure 36 and Figure 37. The battery is located on the backside. The integrated circuit, components and the MIM diode are located on the front side.

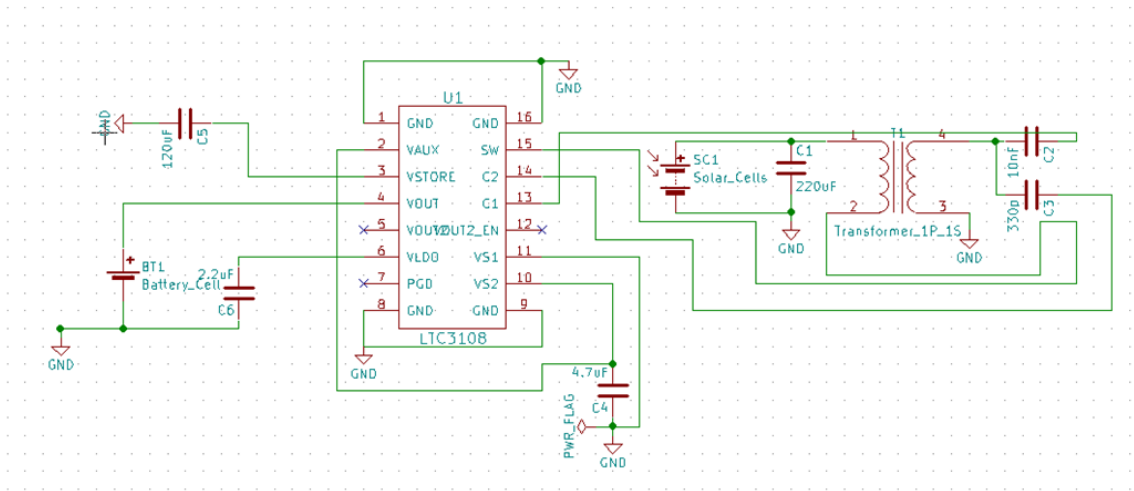


Figure 34 Schematic of the converter module design

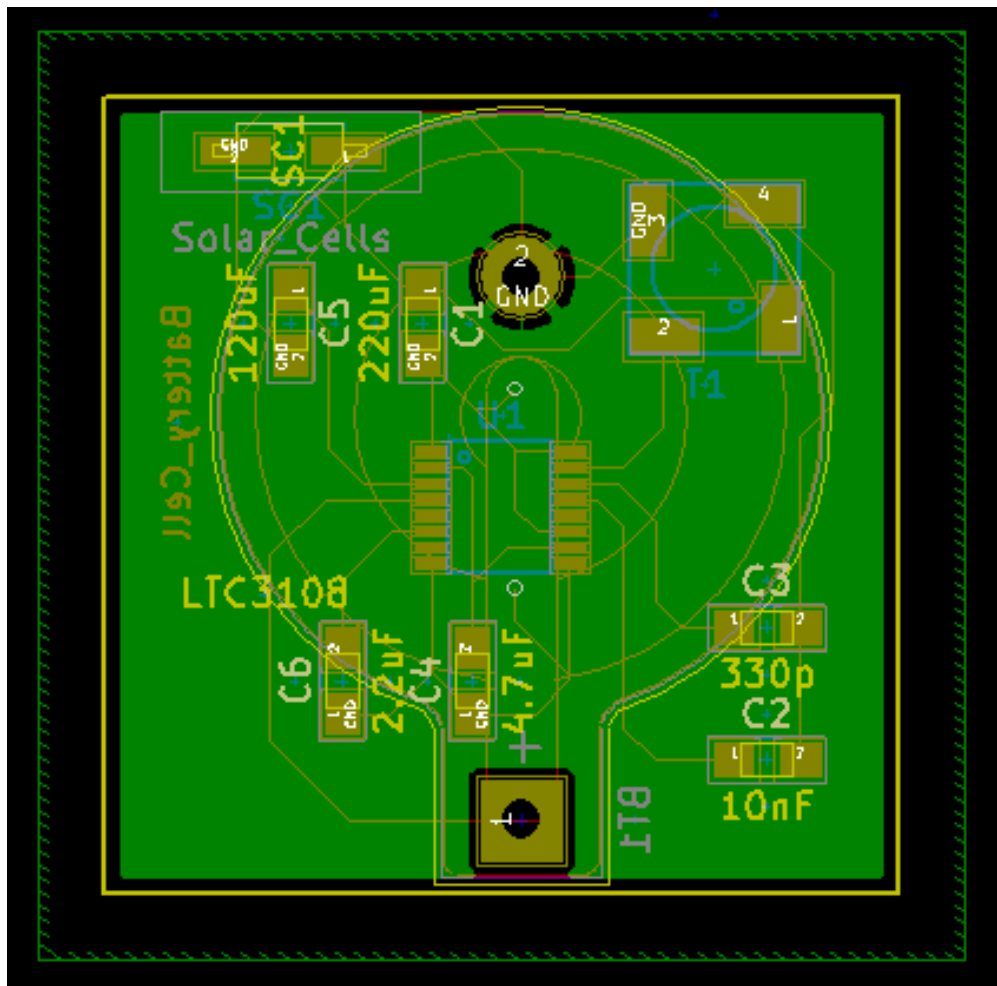


Figure 35 The layout of the converter module design

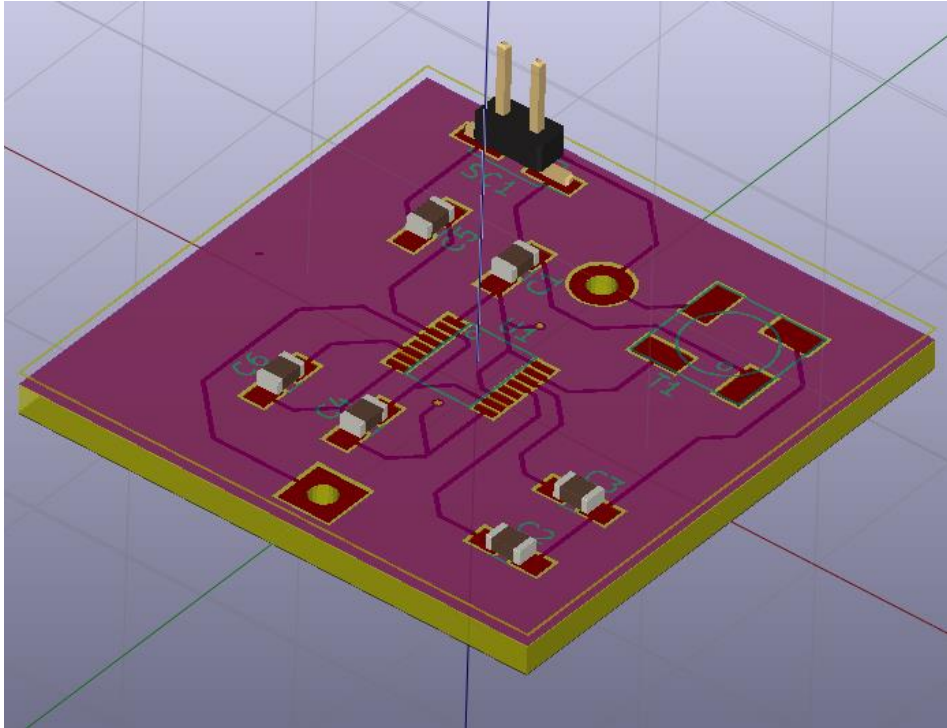


Figure 36 Frontside of the 3 D model of the design

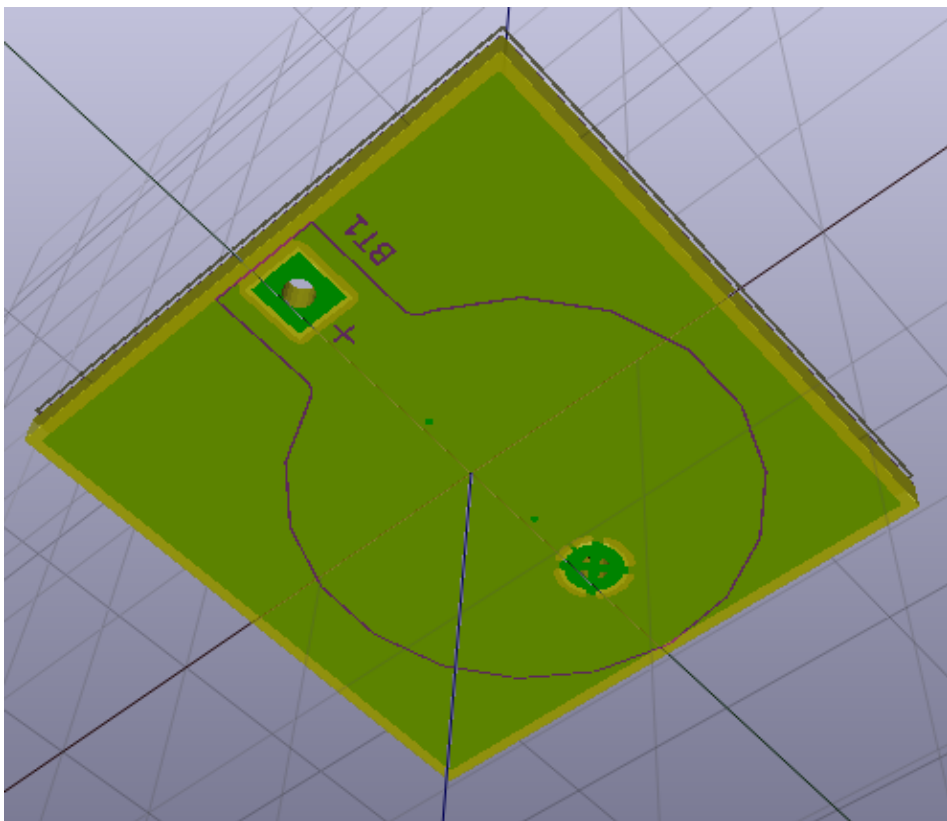


Figure 37 The backside of the 3 D model of the design

4.3. Measurement Results

The MIM diodes were measured with the converter module. Firstly, the MIM is connected directly to the input of the module. However, the input impedance of the module is around 10Ω on the other hand; the structure has an $M\Omega$ range output impedance. Therefore, the output voltage of the MIM diode could not be transferred to the converter module. The impedance matching between the converter module and the MIM diode should be done.

The MIM diode is connected to a unity gain buffer circuit. The unity gain buffer circuit is built with UA 741 opamp. The unity gain buffer circuit has high input impedance and low output impedance. Hence, $M\Omega$ range output impedance is stepped down to output impedance of the buffer circuit, 75Ω stated in the datasheet of UA 741. The open circuit voltage of the MIM diode under optical radiation is 25 mV. Although the output voltage at the end of the buffer is still 25mV, because of a slight mismatch the voltage decreases to 3mV.

The output of the MIM diode is planned to boost with low noise instrumentation amplifier design used for efficiency calculation. The output voltage of the MIM is firstly boosted with ten gain to 250mV, then is transferred to the converter module via unity gain buffer. The converter module gets 30 mV which is suitable for driving the integrated circuit and charging the battery.

The block diagram of the matching circuit is shown in Figure 38. Moreover, Figure 39 presents the measurement setup and the result. The output voltage of the converter measured by multimeter is 5V as it can be seen from Figure 40.

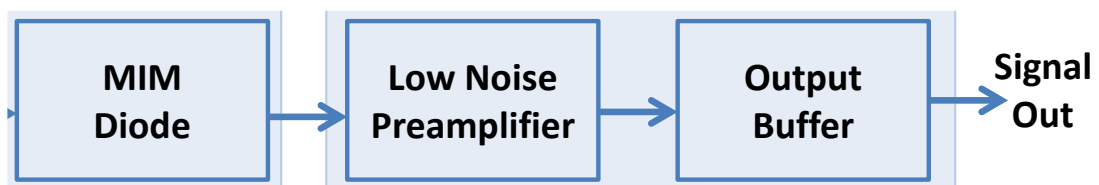


Figure 38 The diagram of the matching circuit.

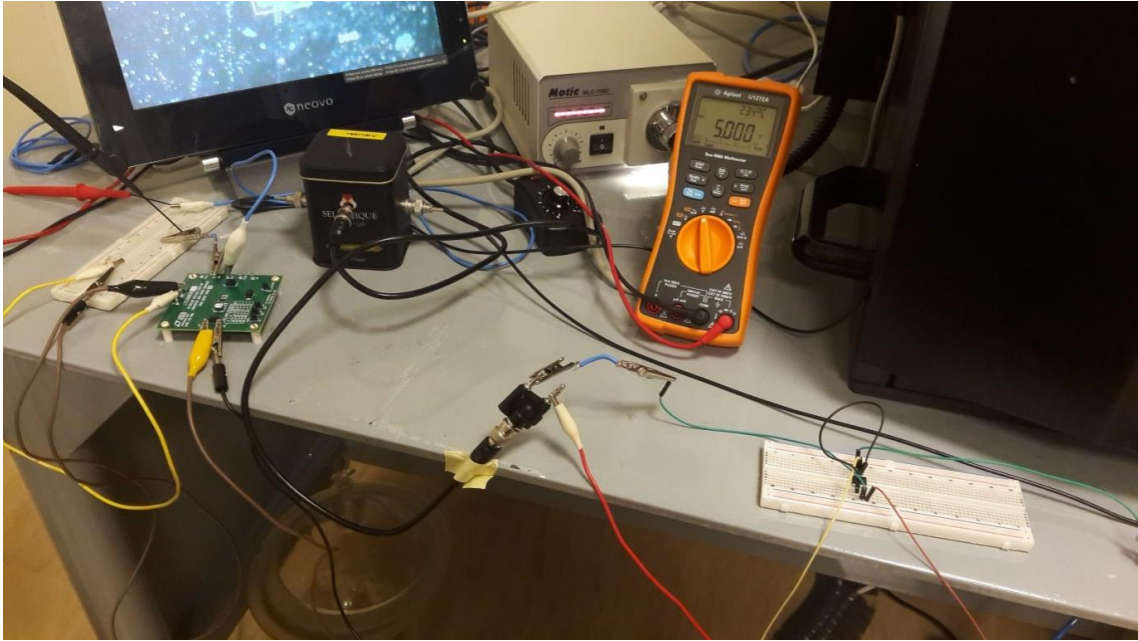


Figure 39 The measurement result of the converter module that multimeter show 5V

5. Conclusion & Future Work

5.1. Summary of Work

Previous researches indicate that hot electron based photovoltaic devices are a potential candidate for solar energy harvesting. In this thesis, I have shown that MIM diodes, in which the current is generated by the tunneling of photon-induced hot electrons, can be utilized as photovoltaic devices. The possible feasibility of the MIM diodes for solar cell application has been investigated experimentally.

I have fabricated different MIM diodes. Firstly, single MIM diodes with different material selection have been explored regarding the optical response. The first investigation was the effect of the barrier height formed between metals and the insulator layer on the performance of the MIM diode. For this purpose, Au/Al₂O₃/Ni and Au/ZnO/Ni material selections were used. I have concluded that low barrier height results in high quantum tunneling in dark condition hence the dark current of low barrier height structure is high. On the other hand, illumination modulates the barrier height and creates optical response. The optical response of higher barrier height structure is more than the low barrier height as a result of a decrease in tunneling distance. The second observation is that the asymmetric barrier formation of the metals and the insulator layer generates a high optical response in comparison to symmetric barrier formation, Cr/HfO₂/Ni MIM diode has been fabricated to explore this. Cr/HfO₂/Ni structure has the highest optical response attributed to higher tunneling probability because of the asymmetry.

I have explored array implementation of the MIM diode. 10x10 array has been constructed with Cr/HfO₂/Ni structure in order to investigate enhancement in the performance. The single structures have been connected in parallel. Moreover, to verify that the optical response is originated by MIM diode, without MIM diodes have been designed by removing active part of the MIM diodes. The contribution of the without MIM diode to optical response has been determined as negligible in comparison to MIM diode's optical response.

The fabrication of the structures has been performed in the Nanotechnology Center in Sabanci University. The process contains cleaning, Electron Beam Lithography (EBL), Physical Vapor Depositions, lift off and inspection. I used EBL to pattern nano-scale features. I deposited metals with e-beam and thermal evaporation deposition techniques.

However, for the performance of the MIM diodes, the insulator material is the decisive part of the structure. The insulator layer should be deposited in a few nanometer thicknesses for high quantum probability. Moreover, the layer should be deposited uniformly. In order to obtain stable and uniform thin insulator layer, Atomic Layer Deposition (ALD) technique has been implemented.

The characterizations of the devices have been carried out regarding different aspects. EDX spectroscopy, SEM inspection, and Ellipsometry Analysis were the method that I used to characterize my devices physically. The oxide quality, material existence, and possible fabrication defect have been investigated. Then, DC characterizations have been performed. I obtained I-V curves, and the current had increasing behavior concerning the optical intensity that refers to optical response. The responsivity of the structure has been extracted.

The conversion efficiency is a prior parameter to evaluate performance. During DC characterization, I applied a bias voltage to measure current. In other words, I gave DC energy for I-V characteristic. Therefore optical response includes a voltage bias effect. The photon generated current should be isolated from voltage and transfer to a load to find output power. I designed a load box to find photon generated current under no bias condition. I calculated efficiency with this load box. For single structure, Cr/HfO₂/Ni formation led 18% efficiency as the 10x10 reached 29% efficiency under optical radiation.

Transferring DC output power to a load is a method to decide that the MIM diode generates DC with optical radiation. However, to demonstrate the MIM diode as an energy harvester or a solar cell, a converter module to charge a battery has been designed. Although there was a mismatch that causes deteriorate the generated power, with a matching circuit that consists of a low noise boost amplifier and a buffer I obtained measurement results. The results show that MIM solar cell can charge a rechargeable battery.

5.2. Future Work

For future works, the MIM diodes performance can be enhanced by optimizing array formation with larger array size and fewer interconnections. Also, further investigation is needed for device design parameters to obtain an output that can compete with state of the art solar cells. The hot electron photo emission can be used to detect IR radiation with

suitable material selections. Device geometry can be changed to collect radiation efficiently. Thus, more hot electron can be generated.

For the converter module concept, the problem is to match the output impedance of the MIM solar cell to input impedance of the converter module. A matching circuit with passive component instead of using boost amplifier and buffer will be researched.

REFERENCES

- [1] S. Sharma, K. J. Kamlesh, and S. Ashutosh, "Solar cells: in research and applications—a review," *Materials Sciences and Applications*, vol. 6, no. 12, pp. 1145-1155, 2015.
- [2] Y. Chu and P. Meisen, "Review and comparison of different solar energy technologies," *Global Energy Network Institute (GENI), San Diego, CA*, 2011.
- [3] T. Tiedje, E. Yablonovitch, G. D. Cody and B. G. Brooks, "Limiting efficiency of silicon solar cells," *IEEE Transactions on electron devices*, vol. 31, no. 5, pp. 711-716, 1984.
- [4] M. Wolf, "Limitations and possibilities for improvement of photovoltaic solar energy converters: Part I: Considerations for earth's surface operation," *Proceedings of the IRE*, vol. 48, no. 7, pp. 1246-1263, 1960.
- [5] W. Shockley and H. J. Queisser, *J. Appl. Phys.*, vol. 32, pp. 510, 1961.
- [6] C. H. Henry, *J. Appl. Phys.*, vol. 51, pp. 449, 1980.
- [7] B. Eliasson, "Metal-Insulator-Metal Diodes for Solar Energy Conversion," *University of Colorado at Boulder*, 2001.
- [8] M. Jacoby, "The future of low-cost solar cells," *Chemical & Engineering News*, vol. 94, pp. 30-35, 2016.
- [9] K. Yoshikawa, H. Kawasaki, W. Yoshida, et al., "Silicon heterojunction solar cell with interdigitated back contacts for a photoconversion efficiency over 26%," *Nature Energy*, vol. 2, no. 5, 2017.
- [10] J. Benick, A. Richter, R. Müller, et al., "High-efficiency n-type HP mc silicon solar cells," *IEEE J photovoltaics*, vol. 7, no. 5, pp. 1171-1175, 2017.
- [11] T. D. Lee and A. U. Ebong, "A review of thin film solar cell technologies and challenges," *Renewable and Sustainable Energy Reviews*, vol. 70, pp. 1286-1297, 2017.
- [12] J. L. Wu, Y. Hirai, T. Kato, H. Sugimoto and V. Bermudez, "New world Record efficiency up to 22.9% for Cu (In,Ga)(Se,S)₂ thin-film solar cell", *7th World Conference on Photovoltaic Energy Conversion (WCPEC-7)*, June 2018.
- [13] L. S. Mattos, S. R. Scully, M. Syfu, E. Olson, L. Yang, C. Ling, B. M. Kayes and G. He, "New module efficiency record: 23.5% under 1-sun illumination using thin-film single-junction GaAs solar cells", *Proceedings of the 38th IEEE Photovoltaic Specialists Conference*, 2012.

- [14] M. Wanlass, "Systems and methods for advanced ultra-high-performance InP solar Cell," *US Patent 9,590,131 B2*, 7 March 2017.
- [15] T. Matsui, A. Bidiville, H. Sai, et al. "High-efficiency amorphous silicon solar cells: Impact of deposition rate on metastability," *Appl Phys Lett.*, vol. 106, no. 5, 2015.
- [16] "Press Release", *Fraunhofer Institute for Solar Energy Systems*, December 2014.
- [17] "Press Release", *NREL NR-4514*, 16 December 2014.
- [18] M. A. Green, Y. Hishikawa, E. D. Dunlop, D. H. Levi, J. Hohl-Ebinger and A. W. Y. Ho-Baillie, "Solar cell efficiency tables (version 52)", *Prog Photovolt Res Appl*, vol. 26, pp. 427-436, 2018.
- [19] "Best Research-Cell Efficiencies", [Online]. Available: <https://www.nrel.gov/pv/>. [Accessed: 3-Jul-2018].
- [20] W. S. Yang, J. H. Noh and N. J. Jeon, "High-performance photovoltaic perovskite layers fabricated through intramolecular exchange," *Science*, vol. 348, no. 6240, pp. 1234-1237, 2015.
- [21] W. C. Brown and R. H. George, "Rectification of Microwave Power," *IEEE Spectrum*, pp. 92–97, Oct. 1964.
- [22] J. G. Simmons, "Electric tunnel effect between dissimilar electrodes separated by a thin insulating film," *J. Appl. Phys.*, vol. 34, pp. 2581-2590, 1963.
- [23] J. G. Simmons, "Generalized formula for the electric tunnel effect between similar electrodes separated by a thin insulating film", *J. Appl. Phys.*, vol. 34, pp. 1793-1803, 1963.
- [24] E. Wisendanger and F.K. Kneubühl, "Thin-film MOM-diodes for infrared detection," *Appl. Phys. Lett.*, vol. 27, pp. 343-349, 1977.
- [25] S. Heiblum, J. Wang, and T. K. Whinnery, "Gustafson Characteristics of integrated MOM junctions at dc and AR optical frequencies," *IEEE J. Q. Elect.*, vol. 159, pp. 159-169, 1978.
- [26] I. Wilke, W. Herrmann, and F. K. Kneubühl, "Integrated nanostrip dipole antennas for coherent 30 THz infrared radiation," *Appl. Phys. B*, vol. 58, pp. 87-95, 1994.
- [27] C. C. Fumeaux, D. F. Spenser, and G. D. Boreman, "Microstrip antenna-coupled infrared detector," *Electron. Lett.*, vol. 35, pp. 2166-2167 1999.
- [28] P. Esfandiari, et al., "Tunable antenna-coupled metal-oxide-metal (MOM) uncooled IR detector", *Proc. SPIE*, vol. 5783, pp. 470-482, 2005.

- [29] S. Krishnan, H. La Rosa, E. Stefanakos, S. Bhansali, and K. Buckle, "Design and development of batch fabricatable metal-insulator-metal diode and microstrip slot antenna as rectenna elements," *Sensors and Actuators A: Physical*, vol. 142, no. 1, 40-47, 2008.
- [30] M. N. Gadalla, M. Abdel-Rahman, and A. Shamim, "Design, Optimization, and Fabrication of a 28.3 THz Nano-Rectenna for Infrared Detection and Rectification," *Science Reports*, vol. 4, pp. 1-9, 2014.
- [31] R. L. Bailey, "A proposed new concept for a solar-energy converter," *Journal of Engineering for Power*, vol. 94, no. 2, pp. 73-77, 1972.
- [32] G. Moddel, "Will Rectenna Solar Cells Be Practical?," *Rectenna Solar Cells, New York, USA: Springer*, pp. 3-24, 2013.
- [33] B. Berland, "Photovoltaic technologies beyond the horizon: optical rectenna solar cell," *NREL/SR-520-33263*.
- [34] E. G. Arsoy, M. Inac, A. Shafique, M. Ozcan, and Y. Gurbuz, "The metal-insulator-metal diodes for infrared energy harvesting and detection applications," *Proc. SPIE*, vol. 9819, 2016.
- [35] F. Yesilkoy et al., "A Mid-IR Antenna Integrated with a Geometrically Asymmetrical Metal-Insulator-Metal Rectifying Diode", *Rectenna Solar Cells. New York, USA: Springer*, pp. 163-188, 2013.
- [36] M. Inac, A. Shafique, M. Ozcan, and Y. Gurbuz, "Device characteristics of antenna-coupled metal-insulator-metal diodes (rectenna) using Al₂O₃, TiO₂, and Cr₂O₃ as insulator layer for energy harvesting applications", *In Thin Films for Solar and Energy Technology VII*, vol. 9561, pp. 95610, September 2015.
- [37] Z. Burshtein and J. Levinson, "Photo-induced tunnel currents in Al-Al₂O₃-Au structures", *Physical Review*, vol. 12, pp. 3453-3457, 1975.
- [38] R. G. Marshalek and F. M. Davidson, "Photoresponse Characteristics of Thin-Film-Nickel-Nickel Oxide-Nickel Tunneling Junctions," *IEEE Journal of Quantum Electronics*, vol. 19, pp. 743-753, 1983.
- [39] M. W. Knight, H. Sobhani, P. Nordlander and N. J. Halas, "Photodetection with Active Optical Antennas," *Science*, vol. 332, pp. 702-704, 2011.
- [40] H. Chalabi, D. Schoen, and M. L. Brongersma, "Hot-Electron Photodetection with a Plasmonic Nanostripe Antenna," *Nano Letters*, vol. 14, pp. 1374-1380, 2014.
- [41] F. Wang and N. A. Melosh, "Plasmonic Energy Collection through Hot Carrier Extraction," *Nano Letters*, vol. 11, pp. 5426-5430, 2011.

- [42] M. L. Brongersma, N. J. Halas, and P. Nordlander, "Plasmon-induced hot carrier science and technology," *Nature Nanotechnology*, vol. 10, pp. 25-34, 2015.
- [43] J. D. Livingston, *Electronic properties of engineering materials*. Wiley New York, NY, 1999.
- [44] S. M. Sze, *Physics of Semiconductor Devices*. John Wiley and Sons, 2nd ed., 1981.
- [45] S. Grover and G. Moddel, "Engineering the current-voltage characteristics of metal-insulator-metal diodes using double-insulator tunnel barriers," *Solid. State. Electron.*, vol. 67, no. 1, pp. 94–99,
- [46] K. Choi et al., "A Focused Asymmetric Metal–Insulator–Metal Tunneling Diode: Fabrication, DC Characteristics, and RF Rectification Analysis," *IEEE Transactions on Electron Devices*, vol. 58, no. 10, pp. 3519-3528, Oct. 2011.
- [47] G. Moddel and S. Grover, "Rectenna solar cells," *Rectenna Sol. Cells*, pp. 1–399, 2013.
- [48] I. E. Hashem, N. H. Rafat, and E. A. Soliman, "Theoretical Study of Metal-Insulator-Metal Tunneling Diode Figures of Merit," *IEEE Journal of Quantum Electronics*, vol. 49, no. 1, pp. 72-79, 2013.
- [49] M. Bareiß, F. Ante, D. Kalblein, G. Jegert, C. Jirauschek, G. Scarpa, B. Fabel, E. M. Nelson, G. Timp, U. Zschieschang, H. Klauk, W. Porod and P. Lugli, "High-Yield Transfer Printing of Metal-Insulator-Metal Nanodiodes," *ACS Nano*, vol. 6, pp. 2853–2859, 2012.
- [50] S. Krishnan, "Design, fabrication, and characterization of thin-film MIM diodes for rectenna array," *University of South Florida*, 2004.
- [51] Fowler, R. H., "The Analysis of Photoelectric Sensitivity Curves for Clean Metals at Various Temperatures," *Physical Review*, vol. 38, no. 1, 1931.
- [52] X. Liu, B. Cuencya and E. A. McFarland "A MIS device structure for detection of chemically induced charge carriers," *Sensors and Actuators B*, vol. 99, pp. 556-561, 2004.
- [53] V. R. A. Holm, B. Y. Zheng, P. M. Denby, B. Holst, N. J. Halas and M. M. Greve, "Work Function-Driven Hot Electron Extraction in a Bimetallic Plasmonic MIM Device," *ACS Photonics*, vol. 5, pp. 1202-1207, 2018.
- [54] H. B. Michaelson, "The work function of the elements and its periodicity," *Journal of Applied Physics*, vol. 48, no. 11, pp. 4729-4733, 1977.

- [55] Y. C. Yeo, T. J. King, and C. Hu, "Metal-dielectric band alignment and its implications for metal gate complementary metal-oxide-semiconductor technology", *Journal of Applied Physics*, vol. 92, no. 12, pp. 7266–7271, 2002.
- [56] V. D. Moravec, S. A. Klopčič, B. Chatterjee, and C. C. Jarrold, "The electronic structure of ZnO and ZnF determined by anion photoelectron spectroscopy," *Chemical Physics Letters*, vol. 341, pp. 313–318, 2001.
- [57] S. Monaghan, P. K. Hurley, K. Cherkaoui, M. A. Negara, and A. Schenk, "Solid-State Electronics Determination of electron effective mass and electron affinity in HfO₂ using MOS and MOSFET structures," *Solid State Electron.*, vol. 53, no. 4, pp. 438–444, 2009.
- [58] J. Luo, M. Boutell and C. Brown, "LTC3108-Ultralow Voltage Step-Up Converter and Power Manager," *Data Sheet*, vol. 23, no. 2, pp. 1-20, 2010.